Eur. J. Mineral., 36, 11–29, 2024
https://doi.org/10.5194/ejm-36-11-2024

European Journal of Mineralogy
Open Access

Multiple growth of zirconolite in marble (Mogok metamorphic belt, Myanmar): evidence for episodes of fluid metasomatism and Zr–Ti–U mineralization in metacarbonate systems

Qian Guo[1,2,3], **Shun Guo**[1,2], **Yueheng Yang**[1,2], **Qian Mao**[1,2], **Jiangyan Yuan**[1,2], **Shitou Wu**[1,2], **Xiaochi Liu**[1,2], **and Kyaing Sein**[4]

[1]State Key Laboratory of Lithospheric Evolution, Institute of Geology and Geophysics, Chinese Academy of Sciences, P.O. Box 9825, Beijing 100029, China
[2]Innovation Academy for Earth Science, Chinese Academy of Sciences, Beijing 100029, China
[3]College of Earth and Planetary Sciences, University of Chinese Academy of Sciences, Beijing 100049, China
[4]Myanmar Geosciences Society, Hlaing University Campus, Yangon, Myanmar

Correspondence: Shun Guo (guoshun@mail.iggcas.ac.cn)

Received: 16 February 2023 – Revised: 9 October 2023 – Accepted: 31 October 2023 – Published: 5 January 2024

Abstract. Fluid infiltration into (meta-)carbonate rocks is an important petrologic process that induces metamorphic decarbonation and potential mineralization of metals or nonmetals. The determination of the infiltration time and the compositional features of reactive fluids is essential to understand the mechanism and process of fluid–rock interactions. Zirconolite (ideal formula: $CaZrTi_2O_7$) is an important U-bearing accessory mineral that can develop in metasomatized metacarbonate rocks. In this study, we investigate the occurrence, texture, composition, and chronology of various types of zirconolite from fluid-infiltrated reaction zones in dolomite marbles from the Mogok metamorphic belt, Myanmar. Three types of zirconolite are recognized: (1) the first type (Zrl-I) coexists with metasomatic silicate and oxide minerals (forsterite, spinel, phlogopite) and has a homogeneous composition with high contents of UO_2 (21.37 wt %–22.82 wt %) and ThO_2 (0.84 wt %–1.99 wt %). (2) The second type (Zrl-II) has textural characteristics similar to those of Zrl-I. However, Zrl-II shows a core–rim zonation with a slightly higher UO_2 content in the rims (average of 23.5 ± 0.4 wt % ($n = 8$)) than the cores (average of 22.1 ± 0.3 wt % ($n = 8$)). (3) The third type (Zrl-III) typically occurs as coronas around baddeleyite and coexists with polycrystalline quartz. Zrl-III has obviously lower contents of UO_2 (0.88 wt %–5.3 wt %) than those of Zrl-I and Zrl-II. All types of zirconolite have relatively low rare earth element (REE) contents ($< 480\,\mu g\,g^{-1}$ for ΣREE). Microtextures and compositions of the three zirconolite types, in combination with in situ zirconolite U–Pb dating using laser ablation inductively coupled plasma mass spectrometry (LA-ICP-MS), reveal episodic fluid infiltration and element mobilization in the dolomite marbles. The first-stage infiltration occurred at ∼ 35 Ma, leading to the formation of Mg-rich silicates and oxides and accessory minerals (Zrl-I, baddeleyite, and geikielite). The reactive fluid was characterized by high contents of Zr, Ti, U, and Th. After that, some Zrl-I grains underwent a local fluid-assisted dissolution–precipitation process, which produced a core–rim zonation (i.e., the Zrl-II type). The final stage of fluid infiltration, recorded by the growth of Zrl-III after baddeleyite, took place at ∼ 19 Ma. The infiltrating fluid of this stage had relatively lower U contents and higher SiO_2 activities than the first-stage infiltrating fluid.

This study illustrates that zirconolite is a powerful mineral that can record repeated episodes (ranging from 35 to 19 Ma) of fluid influx, metasomatic reactions, and Zr–Ti–U mineralization in (meta-)carbonates. This mineral not only provides key information about the timing of fluid flow but also documents the chemical variation in reactive fluids. Thus, zirconolite is expected to play a more important role in characterizing the fluid–carbonate interaction, orogenic CO_2 release, and the transfer and deposition of rare metals.

1 Introduction

Understanding the infiltration of fluids and melts into (meta-)carbonate rocks is of particular importance because these processes can cause significant CO_2 release through fluid/melt-rock interactions during orogenesis (e.g., Evans, 2011; Ferry, 2016; Carter and Dasgupta, 2018; Stewart et al., 2019; Guo et al., 2022) and generate many skarn-type deposits of critical metals (e.g., Kerrick, 1977; Meinert, 1992; Meinert et al., 2005; Deng and Wang, 2016; Xie et al., 2021) and colored gemstones (e.g., Themelis, 2008; Searle et al., 2020; Guo et al., 2021). Precisely dating the fluid infiltration events and constraining the compositions of reactive fluids are critical for understanding the duration and episodes of fluid flow, fluid–carbonate interaction progress, sources of fluids, and ore-forming processes (Yuan et al., 2008; Deng et al., 2014; Zhang et al., 2022). The influx of reactive fluids and melts in magmatic–hydrothermal–metasomatic systems might be episodic and was likely to occur at various stages and under various pressure–temperature conditions (e.g., Barker et al., 2006; Brice et al., 2019; Guo et al., 2021). Clarifying the fluid infiltration history and characterizing the reactive fluid behavior in the metasomatic metacarbonate system are thus highly challenging.

The occurrence of Zr-bearing or Ti-bearing phases provides a good opportunity to uncover the complex infiltration history in carbonate rocks. Zirconolite (ideal formula: $CaZrTi_2O_7$) occurs as an accessory mineral in a variety of lithologies, not only in metasomatized carbonate rocks (Gieré, 1986; Gieré, 1990; Gieré and Williams, 1992; Zaccarini et al., 2004) but also in many SiO_2-poor magmatic rocks, such as carbonatites, kimberlites, alkaline rocks, and lunar basalts (Williams and Gieré, 1996; Giére et al., 1998). In metasomatized marbles, zirconolite develops in various reaction zones and typically shows complex chemical zonation (e.g., Gieré and Williams, 1992). This mineral coexists with other metasomatic minerals (e.g., baddeleyite, geikielite, thorianite, uraninite, titanite, and spinel) and grew by the crystallization from the reactive fluids or the replacement of other Zr–Ti phases (Gieré and Williams, 1992; Zaccarini et al., 2004; Proyer et al., 2014). Importantly, zirconolite typically has high U and Th contents (up to 24 wt % and 22 wt %, respectively), low common Pb contents, and a high U–Pb isotopic system closure temperature of $\sim$ 800–900 °C (Rasmussen and Fletcher, 2004; Wu et al., 2010), which make it an ideal geochronometer of fluid flow and metasomatism.

In addition to Th and U, several groups of trace elements can be incorporated into the structure of zirconolite. For example, the Ca site can be substituted by rare earth elements (REEs); the Ti site can be substituted by some high-field-strength elements (Nb and Ta), Fe, Cr, Al, Zn, and Mg; and the Zr site can be substituted by Hf (Gieré et al., 1998). The enrichment or depletion of different elements in zirconolite is closely associated with the lithology of the host rock, formation setting, and growth stage (Gieré et al., 1998), which allows the compositional signatures of the reactive fluid/melt to be constrained (e.g., Gieré and Williams, 1992; Zaccarini et al., 2004). Therefore, the investigation of zirconolite potentially provides key information on the time-resolved fluid infiltration history and compositional variation of reactive fluids in (meta-)carbonate rocks.

In this study, we investigate the occurrence, texture, mineral compositions, and chronology of different types of zirconolite in fluid-infiltrated marbles from the Mogok metamorphic belt (MMB, central Myanmar). Our results reveal multistage growth of zirconolite, which was caused by episodic fluid infiltration and Zr–Ti–U mineralization events at ages ranging from $\sim$ 35 to $\sim$ 19 Ma. Moreover, we compare and summarize the compositional signatures of zirconolites from various lithologies.

2 Geological setting and sample petrography

The MMB is located in central Myanmar (Fig. 1a). This narrow sickle-shaped belt extends approximately 1500 km from the Andaman Sea north to the eastern Himalayan syntaxis and is distributed along the northwestern margin of the Shan Plateau and southward between the Shan scarp and Sagaing fault (e.g., Barley et al., 2003; Gardiner et al., 2015; Mitchell et al., 2007; Searle et al., 2007, 2017). The formation and evolution of the MMB are closely related to the closure of the Neo-Tethys ocean, India–Asia collision, and post-collision extension and uplift (Searle et al., 2017). The MMB is mainly composed of various types of amphibolite-to-granulite-facies metasedimentary and metaigneous rocks (e.g., Mitchell et al., 2012; Searle et al., 2017) and considered to represent the exhumed lower and middle crustal metamorphic rocks of the Sibumasu (Asia) plate. This belt produces some of the world's best examples of colored gemstones, such as spinel, ruby, and sapphire (e.g., Searle et al., 2007, 2017; Guo et al., 2021; Zhang et al., 2021).

The main lithologies of the MMB include various types of gneisses, migmatites, marbles, schists, and calc–silicate rocks (Mitchell et al., 2007; Searle et al., 2017). In addition, syenites, granitoid rocks, dikes, leucosomes, pegmatites, and hydrothermal veins were widely observed in the MMB (Mitchell et al., 2007; Gardiner et al., 2015; Searle et al., 2017, 2020). In contacts between the magmatic rocks and marbles, metasomatic rocks develop by the influx of fluids or melts, leading to the formation of gemstone-bearing reaction zones (e.g., Themelis, 2008; Guo et al., 2016, 2021; Searle et al., 2020). The peak metamorphic pressures and temperatures of the MMB rocks range from 5 to 12 kbar and from 625 to > 950 °C (Searle et al., 2007; Yonemura et al., 2013; Win et al., 2016; Thu and Enami, 2018; Chen et al., 2021; Lamont et al., 2021). Ultrahigh-temperature metamorphism (> 900 °C)

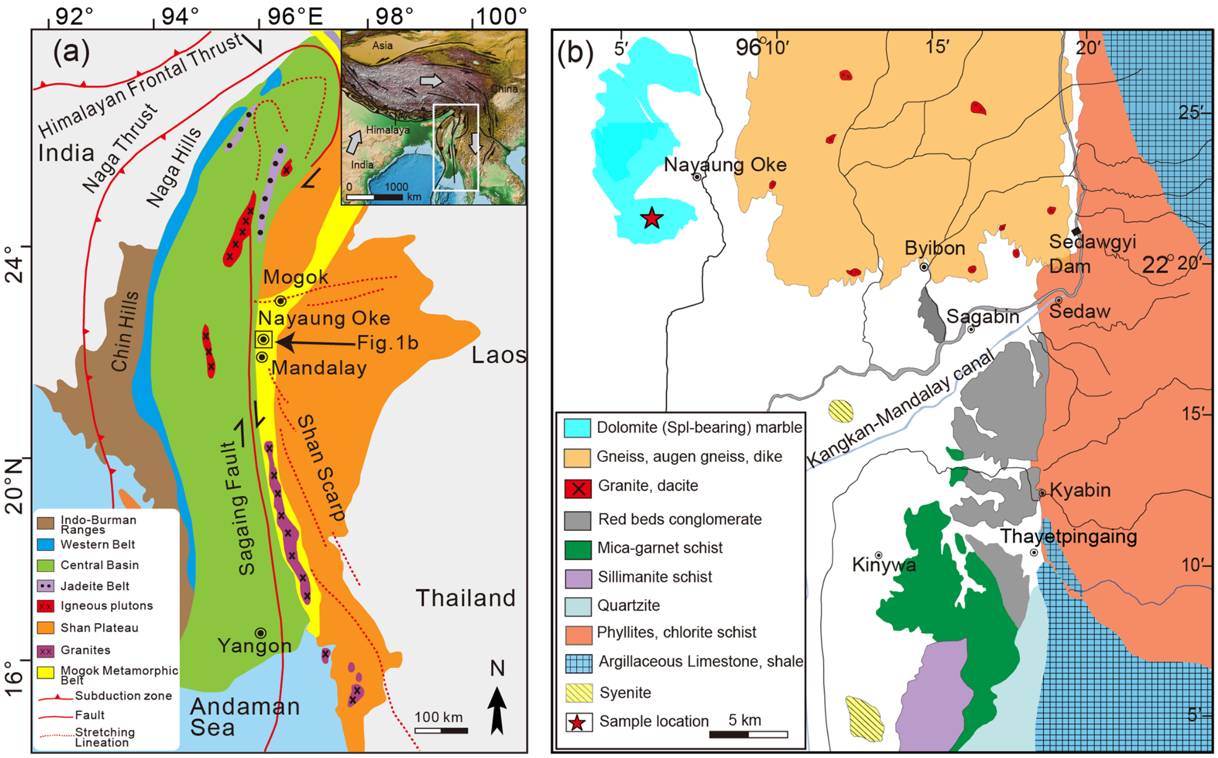

Figure 1. (a) Geological map (modified from Themelis, 2008) showing the distribution of the Mogok metamorphic belt (MMB). **(b)** A simplified geological map (modified from Guo et al., 2021) of the Nayaung Oke area showing the lithologic distribution and sample locality.

has been documented in the Thabeikkiyin and Bernardmyo areas (Chen et al., 2021; Lamont et al., 2021).

The metamorphic ages of the MMB range from ∼ 60 to 20 Ma (Searle et al., 2017; Lamont et al., 2021). Many studies revealed multiple metamorphic ages for single MMB rocks, indicating a multistage metamorphic evolution of these rocks (e.g., Win et al., 2016; Lamont et al., 2021). Ultrahigh-temperature metamorphism was determined to have occurred at 43–32 Ma (Lamont et al., 2021) and ∼ 25 Ma (Chen et al., 2021). New U–Pb dating for zircon or titanite indicates that metamorphism related to ruby formation occurred at 22–25 Ma (Zhang et al., 2021; Phyo et al., 2020). Intrusions of diorites, granite charnockites, and syenites in the MMB have large variations in age ranging from ∼ 170 to 13 Ma (e.g., Mitchell et al., 2012; Searle et al., 2020; Shi et al., 2021). The age of metasomatism (contact metamorphism) varies with the time of infiltrating fluids or melts from these intrusions (Searle et al., 2020; Guo et al., 2021).

The study region is located in the Nayaung Oke area (Fig. 1). This area comprises dolomite marbles, calc–silicate rocks, gneisses, and schists. In addition, small amounts of low-grade metamorphic rocks, sedimentary rocks, and intrusions are present. The Sedawgyi gneisses have a Cambrian U–Pb protolith age of 491 ± 4 Ma, and a biotite granite dike in these gneisses shows a zircon U–Pb age of 17.0 ± 0.3 Ma (Mitchell et al., 2012). Syntectonic deformed hornblende syenites have emplacement ages of 33.11 ± 0.93 to 30.90 ± 0.64 Ma (Barley et al., 2003). In the marbles, polycrystalline mineral reaction zones, which are mainly composed of metasomatic minerals (spinel, forsterite, and phlogopite) and carbonates, have been found (Guo et al., 2021). These reaction zones represent the flow channels of reactive fluids and the products of fluid–marble interactions. Three episodes of fluid influx have been revealed in the reaction zones based on mineral zonations, replacement textures, and baddeleyite–zircon dating (Guo et al., 2021). The first (35–36 Ma) and second (23–24 Ma) infiltration episodes are related to the syenite magmatic events, and the third episode (∼ 17 Ma) is related to the Si-rich fluids derived from the gneisses.

In this study, two samples (13MDL76-A and 13MDL76-B; Guo et al., 2021) of reaction zones in the marbles (Fig. 2a) were investigated. Both samples are composed of calcite (36 vol %–47 vol %), forsterite (18 vol %–36 vol %), spinel (7 vol %–18 vol %), phlogopite (3 vol %–17 vol %), and small amounts of dolomite and accessory minerals (baddeleyite, geikielite, rutile, zirconolite, and uraninite). The two samples have TiO_2 contents of 0.22 wt %–0.35 wt %, Zr contents of 71.1–128 µg g^{-1}, U contents of 65.1–118 µg g^{-1}, and Th contents of 5.17–9.55 µg g^{-1} (Guo et al., 2021). Mineral abbreviations are according to Whitney and Evans (2010), and

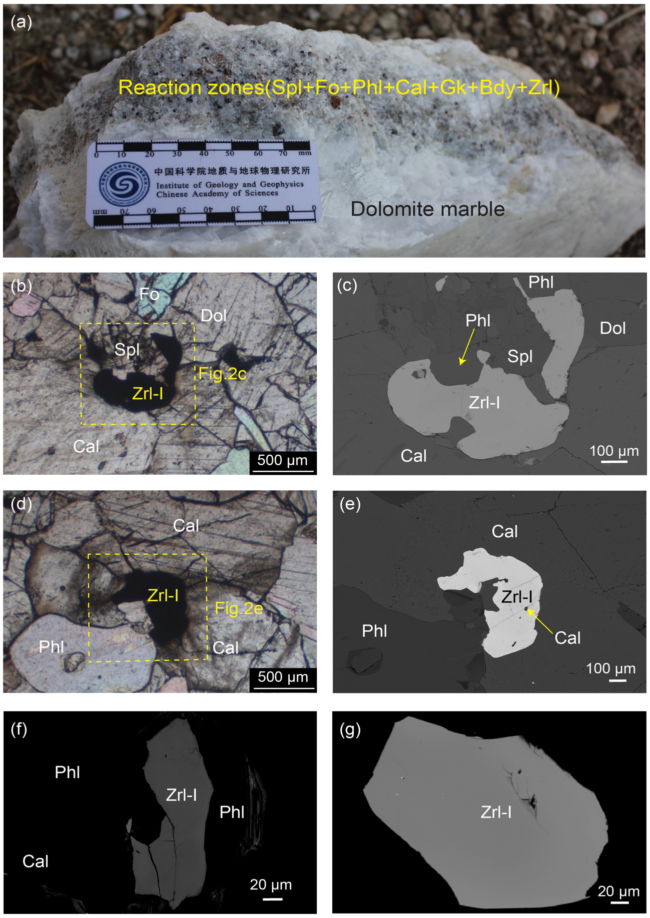

Figure 2. Specimen photograph, photomicrographs (in plane-polarized light), and BSE images of Zrl-I and associated minerals. **(a)** Reaction zones in the marbles. **(b–e)** Zrl-I occurring as irregularly shaped crystals (0.04–10 mm in size) in the matrix of the reaction zones. Coexistence of spinel, forsterite, phlogopite, calcite, and Zrl-I containing calcite inclusions from samples 13MDL76-A **(b–c)** and 13MDL76-B **(d–e)**. **(f–g)** Zrl-I from samples 13MDL76-A **(f)** and 13MDL76-B **(g)** in the resin mount. There is no obvious compositional zonation in Zrl-I.

zirconolite and uraninite are abbreviated as Zrl and Urn, respectively.

3 Analytical methods

3.1 Microtexture and X-ray mapping

The petrographic observations were conducted on thin sections using an optical microscope and a Zeiss Gemini 450 field-emission scanning electron microscope (FE-SEM) equipped with an X-ray energy dispersive spectrometer and a pneumatically retractable backscattered electron (BSE) system at the Institute of Geology and Geophysics, Chinese Academy of Sciences (IGGCAS). The observations, BSE image acquisition, and compositional maps were operated at accelerating voltages of 15–20 kV, a beam current of 5 nA, and a working distance of 8.5 mm. The X-ray mapping was performed by energy dispersive X-ray spectroscopy (EDS) with a dwell time of 2000 µs per point.

3.2 Mineral compositions by microprobe analyses

The compositions of zirconolite, baddeleyite, geikielite, and rutile were analyzed using a Cameca SX Five field emission electron probe micro-analyzer (EPMA) at IGGCAS. Analyses were operated in wavelength-dispersion mode (WDS) with an acceleration voltage of 20 kV, a beam current of 20 nA, and a beam diameter of 1 µm. The crystals used for element analyses were as follows: one thallium acid phthalate (TAP) crystal for Si, Mg, and Al analyses; one large pentaerythritol (LPET) crystal for Zr, Nb, Ca, K, Sc, Th, U, and Y analyses; one large lithium fluoride (LLIF) crystal for Ti, La, Nd, Mn, Sm, Gd, Er, and Hf analyses; and another LLIF crystal for Fe, Ce, Pr, Eu, Dy, Yb, and W analyses. The peak counting time was 10 s for Si, Mg, Zr, Nb, Ti, Fe, La, Ce, and Mn, and the background counting time was 5 s at the high- and low-energy background positions. For the other elements, the peak counting time was 20 s and the background counting time was 10 s at each site. The following excitation lines and calibrant materials have been used: U – Mα, synthetic U glass; Zr – Lα, zircon; Hf – Lα, synthetic Hf metal; Ti – Kα, rutile; Ca – Kα, rhodonite; Nb – Lα, synthetic Nb_2O_5; Sc – Kα, synthetic Sc_2O_3; W – Lβ, scheelite; Mg – Kα, synthetic MgO; Si – Kα, rhodonite; Mn – Kα, rhodonite; Th – Mα, synthetic Th glass; Al – Kα, K-feldspar; K – Kα, K-feldspar; Fe– Kα, hematite; Y – Lα, synthetic Y glass; La – Lα, synthetic La glass; Ce – Lα, synthetic Ce glass; Pr – Lβ, synthetic Pr glass; Nd – Lα, synthetic Nd glass; Sm– Lβ, synthetic Sm glass; Eu – Lα, synthetic Eu glass; Gd – Lα, synthetic Gd glass; Dy – Lα, synthetic Dy glass; Er – Lβ, synthetic Er glass; and Yb – Lα, synthetic Yb glass. The standard materials used for both U and Th (from P and H Developments Ltd.; https://www.pandhdevelopments.com/, last access: 14 December 2023) were synthesized glasses. The glass standard used for Th analyses contains 7.40 wt % Al, 27.3 wt % Si, 15.8 wt % Ca, 5.18 wt % Th, and 44.6 wt % O; and the glass standard used for U analyses contains 7.42 wt % Al, 27.5 wt % Si, 16.1 wt % Ca, 3.85 wt % U, and 44.9 wt % O. The synthetic standard used for REE analyses was also Si–Al–Ca–O glasses with a single 10 % REE added. Averaged detection limits (3σ) were as follows (concentrations in $\mu g\,g^{-1}$): U – 658, Zr – 507, Hf – 444, Ti – 248, Ca – 73, Nb – 392, Sc – 72, W – 1434, Mg – 110, Si – 145, Mn – 220, Th – 676, Al – 77, K – 73, Fe – 219, Y – 344, La – 651, Ce – 220, Pr – 220, Nd – 220, Sm – 1114, Eu – 397, Gd – 438, Dy – 373, Er – 495, and Yb – 436.

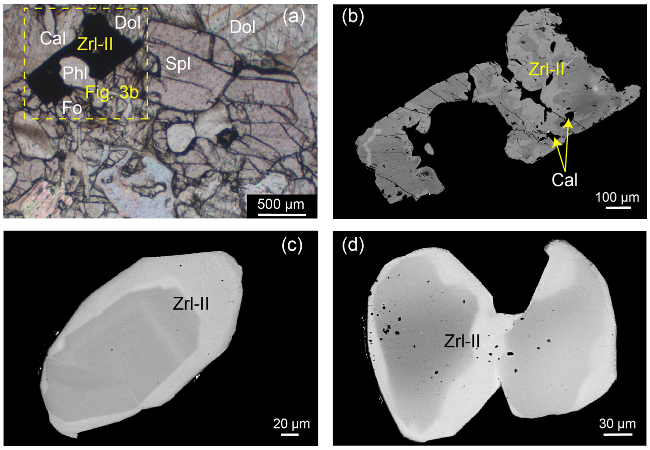

Figure 3. Photomicrographs (in plane-polarized light) and BSE images of Zrl-II and associated minerals. **(a–b)** Zrl-II occurring as irregularly shaped crystals (0.04–10 mm in size) in the matrix of the reaction zones. Coexistence of forsterite, phlogopite, calcite, and Zrl-II containing calcite inclusions from sample 13MDL76-A. **(c–d)** Core–rim zoning structure of Zrl-II from samples 13MDL76-A **(c)** and 13MDL76-B **(d)**.

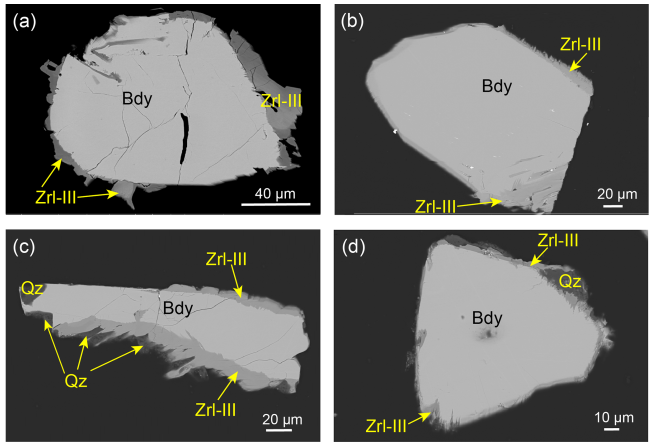

Figure 4. BSE images of Zrl-III (in the rein mount) occurring as small, rounded to platy polycrystalline grains around baddeleyite and forming continuous or discontinuous coronas from samples 13MDL76-B **(a–c)** and 13MDL76-A **(d)**. **(a–b)** Zrl-III coronas that extend into the interior of baddeleyite along some fine fractures. **(c–d)** Zrl-III coexisting or intergrown with quartz. The boundaries between the baddeleyite and Zrl-III show either a zigzag shape **(b–d)** or are smooth **(a)**.

The major and minor element compositions of silicates and oxides (forsterite, spinel, and phlogopite) were measured by a JOEL-8100 EPMA at IGGCAS. The measurements were collected in WDS mode with an acceleration voltage of 15 kV, a beam current of 10 nA, and a beam diameter of 1 µm. Natural and synthetic oxides were used as standards. The precision is $\sim 1.5\,\%$ for Ca, Ti, U, and Zr elements (> 5 wt %) but is $\sim 5\,\%$–$20\,\%$ for other elements due to their low concentrations.

3.3 U–Pb ages of zirconolite

Zirconolite U–Pb dating was carried out by laser ablation inductively coupled plasma mass spectrometry (LA-ICP-MS) employing an Agilent 7500a Q-ICP-MS instrument (Agilent Technologies, USA) coupled to a 193 nm ArF excimer laser system (Geolas HD, Lambda Physik, Göttingen, Germany) at IGGCAS. The method and procedure are similar to those described in Xie et al. (2008). Helium was employed as the carrying gas to improve the transporting efficiency of ablated aerosols. The laser beam diameter was 16 µm at a repetition rate of 3 Hz, and the density of energy was $\sim 4.0\,\mathrm{J\,cm^{-2}}$. The Phalaborwa zirconolite reference (SIMS $^{207}\mathrm{Pb}\,/\,^{206}\mathrm{Pb}$ age $= 2067 \pm 9$ Ma, 1s, $n = 16$; Wu et al., 2010) was measured every six sample spot analyses to calibrate Pb / U ratios and U contents. The resulting data were reduced based on the GLITTER program (Griffin et al., 2008). Weighted $^{206}\mathrm{Pb}\,/\,^{238}\mathrm{U}$ mean dates were calculated using the $^{207}\mathrm{Pb}$ correction of common Pb, assuming a common Pb composition corresponding to the two-stage crustal Pb model of Stacey and Kramers (1975). The age calculations and plotting of Tera-Wasserburg diagrams were made using IsoplotR (Vermeesch, 2018).

3.4 Trace element analysis of zirconolite by LA-ICP-MS analyses

Trace element contents of zirconolite were determined by the same instrument used for the measurement of U–Pb isotopes at IGGCAS. The method is similar to those outlined in Wu et al. (2018). The density of energy at the ablation spots was $\sim 4.0\,\mathrm{J\,cm^{-2}}$. The laser beam diameter was 32 µm at a repetition rate of 5 Hz. The spot locations of trace element analyses are close to those of U–Pb isotope analyses. $^{43}\mathrm{Ca}$ was used as the internal standard. The NIST 610 glass standard (Pearce et al., 1997) was used as the calibration material, and the glass standards of ARM-1 (Wu et al., 2019, 2021) and BCR-2G (Rocholl, 1998) were analyzed as unknown samples to monitor the data quality. The resulting data were also reduced based on the GLITTER program (Griffin et al., 2008). For most trace elements ($> 0.10\,\mathrm{\mu g\,g^{-1}}$), the accuracy is better than $\pm 10\,\%$ with an analytical precision (1 RSD, relative standard deviation) of $\pm 10\,\%$.

4 Results

4.1 Occurrence of zirconolite and associated minerals

Several thin sections were prepared from samples 13MDL76-A and 13MDL76-B to examine the occurrences and textures of zirconolite. Moreover, zirconolite and baddeleyite grains were separated from each sample

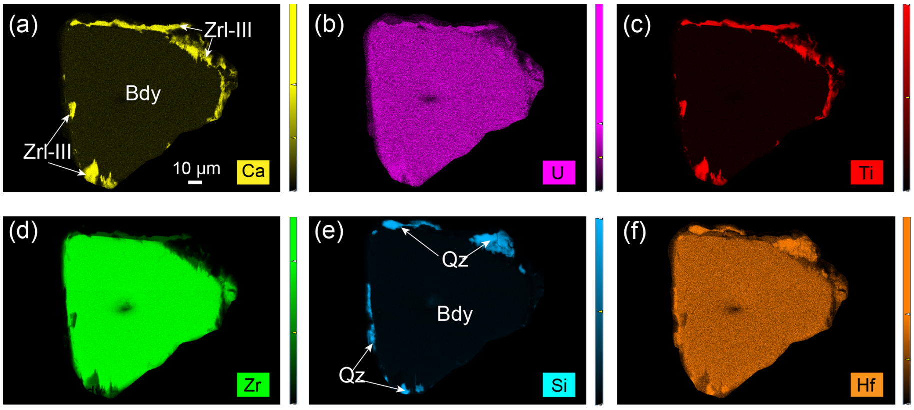

Figure 5. Ca **(a)**, U **(b)**, Ti **(c)**, Zr **(d)**, Si **(e)**, and Hf **(f)** X-ray maps showing the replacement of baddeleyite by Zrl-III in Fig.4d. Zrl-III coexists or is intergrown with quartz **(e)**.

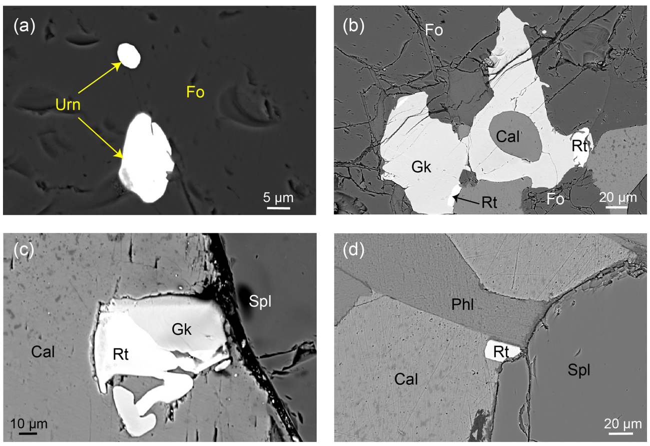

Figure 6. (a) Uraninite inclusions in forsterite from sample 13MDL76-B. **(b–c)** Intergrowth of geikielite and rutile in the matrix from samples 13MDL76-A **(b)** and 13MDL76-B **(c)**. **(d)** Rutile coexisting with spinel, phlogopite, and calcite from sample 13MDL76-A.

and mounted in resins for further observation. Three types of zirconolite were recognized based on their occurrence, texture, and coexisting mineral assemblage.

The first type of zirconolite (Zrl-I) typically occurs as irregularly shaped crystals (0.04–10 mm in size) in the matrix of the reaction zones. Zrl-I coexists with forsterite, spinel, calcite, phlogopite, and dolomite (Fig. 2b–e) and contains calcite inclusions (Fig. 2e). No compositional zonation can be observed in Zrl-I (Fig. 2c, e–g). The second type of zirconolite (Zrl-II) also occurs as an isolated mineral in the matrix. The shape, grain size, coexisting mineral assemblage, and inclusions of Zrl-II are similar to those of Zrl-I (Fig. 3). However, Zrl-II exhibits core–rim zonation. The rims of Zrl-II are brighter than the cores in the BSE images (Fig. 3c and d).

The third type of zirconolite (Zrl-III) exclusively occurs as small, rounded to platy polycrystalline grains around the external edges of baddeleyite and forms continuous or discontinuous coronas that are ≤ 25 µm thick (Fig. 4). We prepared a resin mount of separated baddeleyite to observe Zrl-III (Fig. 4) because baddeleyite can rarely be observed in thin sections. The width of zirconolite around a single baddeleyite grain is highly variable at different locations. The boundaries between the baddeleyite and zirconolite are either zigzag-shaped (Fig. 4b–d) or smooth (Fig. 4a). The original shapes of baddeleyite grains and the reaction interface can be found. The growth of Zrl-III also occurs in the interior of baddeleyite along some fine fractures that extend to the outside of the baddeleyite grains (Fig. 4a). The BSE images (Fig. 4c and d) and element maps (Fig. 5) show that Zrl-III typically coexists with or is intergrown with fragmental, porous, polycrystalline quartz.

Moreover, in both samples, some Ti-bearing and U-bearing accessory minerals, such as geikielite ($MgTiO_3$), rutile (TiO_2), and uraninite (UO_2), can be observed in the matrix or as inclusions in silicate minerals (Fig. 6).

4.2 Mineral compositions

4.2.1 Zirconolite

The compositions of zirconolite are presented in Tables 1 and 2. Zrl-I has 28 wt %–30 wt % ZrO_2, 31 wt %–33 wt % TiO_2, and 8.5 wt %–9.6 wt % CaO (Fig. 7a; Table 1). The UO_2 content of Zrl-I ranges from 21 wt %–23 wt %, and the ThO_2 content ranges from 0.84 wt %–1.99 wt %. Zrl-I also contains small amounts of MgO (2.6 wt %–3.2 wt %), FeO (1.2 wt %–1.3 wt %), Al_2O_3 (0.46 wt %–0.74 wt %), HfO_2 (0.58 wt %–0.72 wt %), Nb_2O_5 (0.37 wt %–0.52 wt %), and Sc_2O_3 (≤ 0.03 wt %) (Fig. 8c; Fig. S1; Table 1). The contents of REEs are very low (generally lower than the limit of detection by EPMA analyses). LA-ICP-MS analyses indicate that the ΣREE of Zr-I ranges from 123 to 174 µg g^{-1} (Fig. 9;

Table 1. Representative major and minor element compositions (wt %) and formulas of different types of zirconolite from the MMB.

	Zirconolite-I								Zirconolite-II								Zirconolite-III					
	13MDL76-A				13MDL76-B				13MDL76-A				13MDL76-B				13MDL76-A		13MDL76-B			
	Grain 1		Grain 2		Grain 1		Grain 2		Grain 1		Grain 2		Grain 1		Grain 2		Grain 1		Grain 1		Grain 2	
									R	C	R	C	R	C	R	C						
WO_3	0.17	0.06	bdl	bdl	bdl	0.05	0.00	0.03	0.27	bdl	bdl	0.06	bdl	bdl	0.08	bdl	bdl	0.22	bdl	0.36	bdl	0.39
Nb_2O_5	0.37	0.40	0.52	0.51	0.40	0.49	0.37	0.50	0.62	0.37	0.49	0.38	0.44	0.52	0.53	0.40	0.96	0.95	1.17	1.30	0.77	0.74
SiO_2	bdl	0.04	bdl	bdl	bdl	bdl	0.02	bdl	bdl	bdl	bdl	bdl	bdl	0.03	bdl	0.03	0.03	0.08	b.d.	0.07	0.05	0.05
TiO_2	32.75	32.41	31.10	31.04	31.51	30.67	31.49	31.79	30.52	31.74	31.15	31.80	30.69	31.36	30.73	30.38	42.18	42.49	36.71	39.81	42.64	43.76
ZrO_2	29.75	29.36	28.25	29.23	28.80	29.02	28.97	28.92	28.16	29.39	27.85	28.84	28.53	29.20	28.08	29.51	32.53	34.41	33.95	37.50	36.44	35.96
HfO_2	0.70	0.66	0.72	0.58	0.62	0.71	0.65	0.69	0.75	0.68	0.62	0.76	0.67	0.67	0.76	0.65	0.93	1.03	1.03	1.03	0.94	1.02
ThO_2	0.84	0.88	1.86	1.25	0.79	1.99	1.29	0.84	1.20	0.87	1.38	0.71	1.63	0.91	1.42	1.96	1.20	1.76	6.84	3.15	0.90	0.60
UO_2	21.37	21.53	22.79	22.50	22.40	22.81	22.82	22.25	24.00	21.83	23.33	22.31	23.42	21.69	24.01	22.35	5.28	0.67	4.98	0.95	1.73	0.88
Al_2O_3	0.71	0.68	0.50	0.61	0.63	0.46	0.65	0.74	0.53	0.68	0.49	0.72	0.49	0.64	0.52	0.56	0.61	0.52	0.67	0.77	0.59	0.57
Sc_2O_3	0.03	bdl	bdl	bdl	bdl	bdl	bdl	bdl	bdl	bdl	0.03	bdl	bdl	bdl	bdl	bdl	0.03	bdl	0.03	bdl	0.03	bdl
Y_2O_3	bdl	bdl	bdl	bdl	bdl	bdl	bdl	bdl	0.047	bdl	bdl	bdl	bdl	bdl	bdl	bdl	0.043	0.180	0.041	0.057	bdl	bdl
La_2O_3	bdl	bdl	bdl	bdl	bdl	bdl	bdl	bdl	bdl	bdl	bdl	bdl	bdl	bdl	bdl	bdl	bdl	bdl	bdl	bdl	bdl	0.06
Ce_2O_3	bdl	bdl	bdl	bdl	bdl	bdl	bdl	bdl	bdl	bdl	0.12	bdl	bdl	bdl	bdl	bdl	bdl	0.13	bdl	bdl	bdl	bdl
Pr_2O_3	bdl	bdl	bdl	bdl	bdl	bdl	bdl	bdl	bdl	bdl	bdl	bdl	bdl	bdl	bdl	bdl	bdl	bdl	bdl	bdl	bdl	bdl
Nd_2O_3	bdl	bdl	bdl	bdl	bdl	bdl	bdl	bdl	bdl	bdl	bdl	bdl	bdl	bdl	bdl	bdl	bdl	0.16	bdl	bdl	bdl	bdl
Sm_2O_3	bdl	bdl	bdl	bdl	bdl	bdl	bdl	bdl	0.16	bdl	bdl	bdl	bdl	bdl	bdl	bdl	bdl	bdl	bdl	bdl	bdl	bdl
Eu_2O_3	bdl	bdl	bdl	bdl	bdl	bdl	bdl	bdl	bdl	bdl	bdl	bdl	bdl	bdl	bdl	bdl	bdl	bdl	bdl	bdl	bdl	bdl
Gd_2O_3	bdl	bdl	bdl	bdl	bdl	bdl	bdl	bdl	bdl	bdl	bdl	bdl	bdl	bdl	bdl	bdl	bdl	0.09	bdl	bdl	0.06	bdl
Dy_2O_3	bdl	bdl	bdl	bdl	bdl	bdl	bdl	bdl	bdl	bdl	bdl	bdl	bdl	bdl	bdl	bdl	bdl	bdl	bdl	bdl	bdl	bdl
Er_2O_3	bdl	bdl	bdl	bdl	bdl	bdl	bdl	bdl	bdl	bdl	bdl	bdl	bdl	bdl	bdl	bdl	bdl	bdl	bdl	bdl	bdl	bdl
Yb_2O_3	bdl	bdl	bdl	bdl	bdl	bdl	bdl	bdl	bdl	bdl	bdl	bdl	bdl	bdl	bdl	bdl	bdl	bdl	bdl	bdl	bdl	bdl
CaO	9.63	9.60	8.51	8.95	9.30	8.65	9.16	9.06	8.73	9.49	8.89	9.30	8.86	9.33	9.01	8.99	15.07	14.77	12.48	14.48	15.13	15.13
MgO	2.57	2.74	3.22	3.02	2.77	3.08	2.96	2.95	3.00	2.80	2.82	2.73	2.92	2.74	2.94	3.11	0.50	0.24	1.28	0.48	0.27	0.26
MnO	bdl	bdl	bdl	bdl	bdl	bdl	0.03	bdl	bdl	bdl	bdl	0.03	bdl	bdl	0.00	bdl	bdl	0.03	bdl	bdl	bdl	bdl
FeO	1.20	1.20	1.24	1.25	1.17	1.24	1.20	1.16	1.20	1.15	1.24	1.19	1.30	1.12	1.24	1.28	0.59	0.65	1.20	0.73	0.48	0.47
K_2O	bdl	bdl	bdl	bdl	bdl	bdl	bdl	bdl	bdl	bdl	bdl	bdl	bdl	bdl	bdl	bdl	0.01	bdl	bdl	bdl	bdl	bdl
Total	100.09	99.56	98.70	98.93	98.39	99.16	99.59	98.94	99.19	99.00	98.41	98.81	98.94	98.20	99.6	99.20	99.95	98.38	100.36	100.68	100.03	99.88

Table 1. Continued.

	Zirconolite-I								Zirconolite-II								Zirconolite-III					
	13MDL76-A				13MDL76-B				13MDL76-A				13MDL76-B				13MDL76-A		13MDL76-B			
	Grain 1		Grain 2		Grain 1		Grain 2		Grain 1		Grain 2		Grain 1		Grain 2		Grain 1		Grain 1		Grain 2	
									R	C	R	C	R	C	R	C						
	Formulas on the basis of four cations and seven O atoms																					
W	0.003	0.001	bdl	bdl	bdl	0.001	0.001	0.001	0.005	bdl	bdl	0.001	bdl	bdl	0.005	bdl	bdl	0.003	bdl	0.005	bdl	0.006
Nb	0.011	0.012	0.016	0.016	0.012	0.015	0.019	0.02	0.019	0.011	0.015	0.012	0.014	0.011	0.019	0.012	0.026	0.025	0.033	0.035	0.02	0.019
Si	bdl	0.003	bdl	bdl	bdl	bdl	0.001	0.002	bdl	bdl	bdl	bdl	bdl	0.002	bdl	0.002	0.002	0.004	0.001	0.004	0.003	0.003
Ti	1.631	1.625	1.601	1.587	1.612	1.578	1.562	1.566	1.576	1.605	1.612	1.616	1.585	1.607	1.576	1.558	1.876	1.885	1.706	1.759	1.863	1.896
Zr	0.961	0.955	0.943	0.969	0.956	0.968	0.984	0.962	0.943	0.964	0.935	0.951	0.955	0.970	0.943	0.981	0.938	0.990	1.023	1.074	1.032	1.01
Hf	0.013	0.013	0.014	0.011	0.012	0.014	0.011	0.013	0.015	0.013	0.012	0.015	0.013	0.013	0.015	0.013	0.016	0.017	0.018	0.017	0.016	0.017
U	0.315	0.319	0.347	0.34	0.339	0.347	0.354	0.355	0.367	0.327	0.357	0.336	0.358	0.329	0.367	0.339	0.070	0.009	0.068	0.012	0.022	0.011
Th	0.013	0.013	0.029	0.019	0.012	0.031	0.029	0.028	0.019	0.013	0.022	0.011	0.025	0.014	0.019	0.03	0.016	0.024	0.096	0.042	0.012	0.008
Al	0.056	0.054	0.04	0.049	0.051	0.037	0.041	0.042	0.043	0.054	0.04	0.057	0.04	0.052	0.043	0.045	0.042	0.036	0.048	0.053	0.04	0.039
Sc	0.001	bdl	bdl	bdl	bdl	bdl	bdl	bdl	bdl	bdl	0.002	bdl	bdl	bdl	bdl	bdl	0.002	bdl	0.001	bdl	0.001	bdl
Y	bdl	bdl	bdl	bdl	bdl	bdl	bdl	bdl	0.002	bdl	bdl	bdl	bdl	bdl	bdl	bdl	0.001	0.006	0.001	0.002	bdl	bdl
La	bdl	bdl	bdl	bdl	bdl	bdl	0.002	bdl	bdl	bdl	bdl	bdl	bdl	bdl	bdl	bdl	bdl	bdl	bdl	bdl	bdl	bdl
Ce	bdl	bdl	bdl	bdl	bdl	bdl	bdl	bdl	bdl	bdl	0.003	bdl	bdl	bdl	bdl	bdl	bdl	0.003	bdl	bdl	bdl	bdl
Pr	bdl	bdl	bdl	bdl	bdl	bdl	bdl	bdl	bdl	bdl	bdl	bdl	bdl	bdl	bdl	bdl	bdl	bdl	bdl	bdl	bdl	bdl
Nd	bdl	bdl	bdl	bdl	bdl	bdl	bdl	bdl	bdl	bdl	bdl	bdl	bdl	bdl	bdl	bdl	bdl	0.003	bdl	bdl	bdl	bdl
Sm	bdl	bdl	bdl	bdl	bdl	bdl	bdl	bdl	0.004	bdl	bdl	bdl	bdl	bdl	bdl	bdl	bdl	bdl	bdl	bdl	bdl	bdl
Eu	bdl	bdl	bdl	bdl	bdl	bdl	bdl	bdl	bdl	bdl	bdl	bdl	bdl	bdl	bdl	bdl	bdl	bdl	bdl	bdl	bdl	bdl
Gd	bdl	bdl	bdl	bdl	bdl	bdl	bdl	bdl	bdl	bdl	bdl	bdl	bdl	bdl	bdl	bdl	bdl	0.002	bdl	bdl	0.001	bdl
Dy	bdl	bdl	bdl	bdl	bdl	bdl	bdl	bdl	bdl	bdl	bdl	bdl	bdl	bdl	bdl	bdl	bdl	bdl	bdl	bdl	bdl	bdl
Er	bdl	bdl	bdl	bdl	bdl	bdl	bdl	bdl	bdl	bdl	bdl	bdl	bdl	bdl	bdl	bdl	bdl	bdl	bdl	bdl	bdl	bdl
Yb	bdl	bdl	bdl	bdl	bdl	bdl	bdl	bdl	bdl	bdl	bdl	bdl	bdl	bdl	bdl	bdl	bdl	bdl	bdl	bdl	bdl	bdl
Ca	0.683	0.686	0.624	0.652	0.678	0.634	0.63	0.629	0.642	0.684	0.656	0.674	0.652	0.681	0.64	0.657	0.955	0.934	0.826	0.912	0.942	0.934
Mg	0.254	0.272	0.329	0.306	0.280	0.314	0.313	0.327	0.307	0.280	0.289	0.275	0.299	0.278	0.307	0.316	0.044	0.021	0.118	0.042	0.023	0.022
Mn	bdl	bdl	bdl	bdl	bdl	bdl	bdl	0.002	bdl	bdl	bdl	0.001	bdl	bdl	bdl	bdl	bdl	0.002	bdl	bdl	bdl	bdl
Fe	0.066	0.067	0.071	0.071	0.067	0.071	0.059	0.061	0.069	0.065	0.071	0.068	0.074	0.064	0.069	0.073	0.029	0.032	0.062	0.036	0.023	0.022
K	0.000	0.000	0.000	0.000	0.000	0.000	0.000	0.000	0.000	0.000	0.000	0.000	0.000	0.000	0.000	0.000	0.000	0.000	0.000	0.000	0.000	0.000
Total	4.007	4.020	4.014	4.020	4.019	4.010	4.004	4.009	4.011	4.016	4.014	4.017	4.015	4.021	4.003	4.026	4.017	3.996	4.001	3.993	3.998	3.987

bdl: below detection limits. C: core. R: rim.

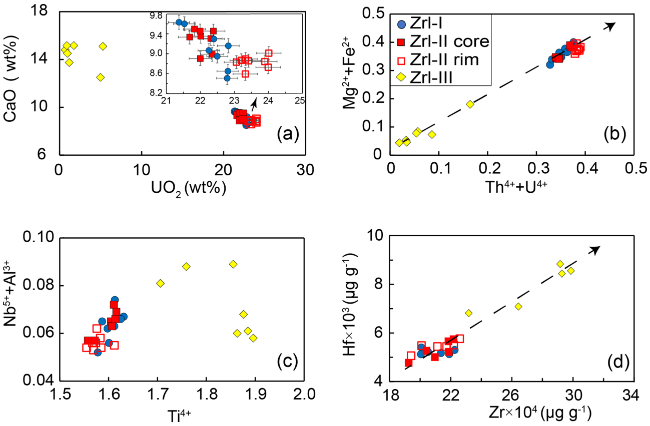

Figure 7. Compositional variations in zirconolite from the MMB. **(a)** Plots of CaO vs. UO_2 (wt %) discriminating between the different types of zirconolite. **(b–d)** Plots of $Mg^{2+} + Fe^{2+}$ vs. $Th^{4+} + U^{4+}$ (apfu) **(b)**, $Nb^{5+} + Al^{3+}$ vs. Ti^{4+} (apfu) **(c)**, and Hf vs. Zr^{4+} ($\mu g\, g^{-1}$) **(d)** showing negative or positive correlations between them.

Table 2). Zrl-I exhibits a light rare earth element (LREE)-depleted and flat heavy rare earth element (HREE) pattern in the chondrite-normalized diagram with negative Eu anomalies (Fig. 9). The Cs, Rb, and Ba contents of Zrl-I are lower than the limits of detection (Table 2).

Zrl-II has ZrO_2 (28 wt %–30 wt %), TiO_2 (30 wt %–32 wt %), CaO (8.6 wt %–9.5 wt %), UO_2 (21 wt %–24 wt %), and ThO_2 (0.71 wt %–2.0 wt %) contents similar to those of Zrl-I (Fig. 7a; Table 1). The brighter rims in the BSE images have slightly higher UO_2 and lower CaO contents than the darker cores (Fig. 7a; Table 1). The contents of MgO, FeO, Al_2O_3, Sc_2O_3, and HfO_2 in both cores and rims are similar (Fig. S1). Both the cores and rims have low REE contents (125 to 158 $\mu g\, g^{-1}$ for ΣREE) and show a LREE-depleted pattern similar to that of Zrl-I (Fig. 9).

Compared to Zrl-I and Zrl-II, Zrl-III is found to have higher contents of ZrO_2 (32 wt %–38 wt %), TiO_2 (36 wt %–44 wt %), CaO (12 wt %–15 wt %), Nb_2O_5 (0.74 wt %–1.3 wt %), and HfO_2 (0.93 wt %–1.04 wt %); much lower contents of UO_2 (0.88 wt %–5.3 wt %); and slightly lower contents of MgO (0.24 wt %–1.3 wt %) and FeO (0.47 wt %–1.2 wt %) (Table 1; Fig. S1). The ThO_2 contents range from 0.60 wt %–6.8 wt %. The Al_2O_3 contents of Zrl-III (0.52 wt %–0.77 wt %) are similar to those of Zrl-I (0.46 wt %–0.74 wt %) and Zrl-II (0.49 wt %–0.72 wt %). The LA-ICP-MS analyses indicate that the contents of REEs in Zrl-III (366 to 477 $\mu g\, g^{-1}$ for ΣREE) are higher than those of Zrl-I and Zrl-II (Fig. 9; Table 2). In the chondrite-normalized diagram, Zrl-III shows a nearly flat REE pattern (except La and Ce) with a negative Eu anomaly (Fig. 9).

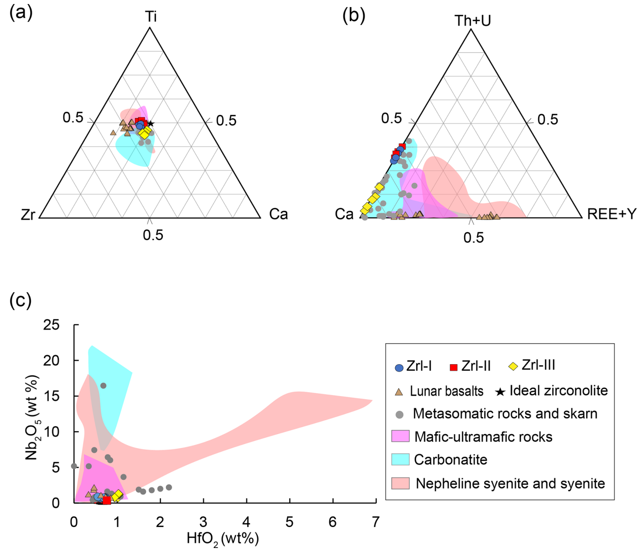

Figure 8. (a) Ca–Ti–Zr compositional variations (apfu) of zirconolite. **(b)** Ca–(Th + U)–(REE + Y) compositional variations (apfu) of zirconolite. **(c)** Plots of Nb_2O_5 vs. HfO_2 (wt %) of zirconolite. Zirconolite from nepheline syenite or syenite (Platt et al.,1987; Ventura et al., 2000; Bellatreccia et al., 2002; Haifler et al., 2017; Melluso et al., 2017), ultra-mafic to mafic rocks (Williams, 1978; Lorand and Cottin, 1987; Stucki et al., 2001; Rajesh et al., 2006; Azzone et al., 2009), carbonatite (Williams and Giere, 1996), metasomatic rocks (Purtscheller and Tessadri., 1985; Gieré, 1986; Gieré and Williams, 1992; Zaccarini et al., 2004; Pascal et al., 2009; Proyer et al., 2014), and lunar basalt (Busche et al., 1972; Li et al., 2021; Wang et al., 2021).

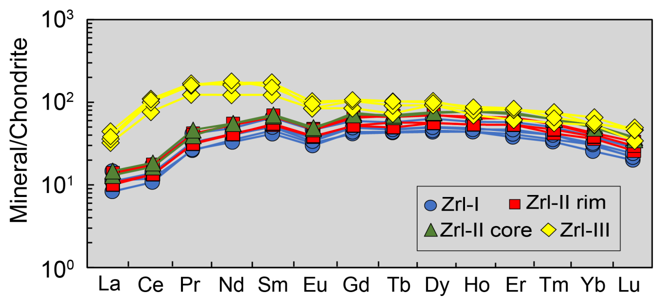

Figure 9. Chondrite-normalized REE patterns (Sun and McDonough, 1989) of different types of zirconolite from the MMB.

4.2.2 Baddeleyite, rutile, and geikielite

The compositions of baddeleyite, rutile, and geikielite measured by EPMA are presented in Table S1. Baddeleyite is mainly composed of ZrO_2 (94 wt %–98 wt %) and HfO_2 (2.3 wt %–5.2 wt %). This mineral also contains minor amounts of TiO_2 (0.18 wt %–0.52 wt %) and Nb_2O_5 (0.13 wt %–0.22 wt %). Rutile is composed of TiO_2 (> 97 wt %) and contains minor amounts of ZrO_2 (0.03 wt %–0.59 wt %), FeO (0.02 wt %–0.09 wt %), CaO (0.07 wt %–1.1 wt %), and Nb_2O_5 ($\leq$ 0.54 wt %). Geikielite

Table 2. Representative trace element compositions of zirconolite (concentrations in $\mu g\,g^{-1}$).

	Zirconolite-I						Zirconolite-II						Zirconolite-III					Averaged detection limits
	13MDL76-A			13MDL76-B			13MDL76-A			13MDL76-B			13MDL76-A			13MDL76-B		
							C	C	R	R	C	C						
Na	1666	1603	1622	1502	1568	1493	1311	1320	1397	1459	1437	1610	987	937	753	1091	1023	4.8
P	bdl	bdl	304	bdl	bdl	bdl	bdl	bdl	bdl	bdl	bdl	bdl	5607	4955	2611	2987	2893	106
K	bdl	bdl	bdl	bdl	bdl	bdl	bdl	bdl	bdl	bdl	bdl	bdl	bdl	bdl	bdl	bdl	bdl	24.7
Sc	173	108	99.1	92.5	97.3	88.3	92.8	98	97.2	95.9	98.1	97.2	126	47.9	88.6	60.7	63.4	27.8
V	526	542	590	533	518	543	534	539	499	478	540	577	182	178	191	180	175	1.8
Cr	94.2	110	80.1	88.4	96.6	73.2	83.0	91.1	90.6	99.2	81.8	211	bdl	bdl	bdl	bdl	bdl	17.2
Mn	76.9	73.9	83.6	64.5	75.2	69.1	62.5	69.5	71.7	68.6	71.6	67.5	24.4	27.0	26.1	42.3	29.8	3.08
Fe	9117	8731	8587	8057	8906	7106	7878	8114	9207	9078	8098	7180	4420	4497	4759	5738	4835	98.4
Zn	20.6	16.1	17.1	15.5	18.2	16.3	17.1	20.5	16.9	21.4	16	13.7	28.1	22.8	10.7	23.2	27.1	7.29
Ga	6.13	7.43	7.75	6.8	5.9	6.95	6.69	6	6.07	5.98	5.93	7.71	7.06	5.5	6.95	6.53	6.47	1.82
Rb	bdl	bdl	bdl	bdl	bdl	bdl	bdl	bdl	bdl	bdl	bdl	bdl	bdl	bdl	bdl	bdl	bdl	0.82
Sr	1.59	1.51	1.76	1.39	1.69	1.68	1.71	1.6	1.55	2.2	1.65	1.86	2.81	2.58	2.08	5.7	3.41	0.57
Nb	2863	2945	2823	2770	2927	2680	2906	2794	3182	3077	2781	2970	3827	4062	4244	4185	4191	0.81
Sn	156	199	176	172	167	164	172	162	192	195	156	190	624	572	641	597	627	1.35
Sb	1.86	3.04	bdl	2.25	2.15	bdl	2.05	1.61	2.7	2.43	1.45	1.43	4.79	bdl	5.24	3.23	3.92	1.85
Cs	bdl	bdl	bdl	bdl	bdl	bdl	bdl	bdl	bdl	bdl	bdl	bdl	bdl	bdl	bdl	bdl	bdl	0.33
Ba	bdl	bdl	bdl	bdl	bdl	bdl	bdl	bdl	bdl	bdl	bdl	bdl	bdl	bdl	bdl	22.2	bdl	1.97
La	5.02	6.35	4.64	4.33	3.72	4.82	4.85	4.22	4.15	4.64	3.84	4.79	12.6	13.8	15.3	18.7	16.3	0.34
Ce	16.3	19.5	15.6	13.8	12.3	15.6	16.4	13.1	13.4	14.9	12.6	16.1	89.2	82.4	106	116	113	0.34
Pr	5.78	6.32	5.02	4.64	4.17	5.03	5.46	4.13	4.37	5.06	4.12	5.35	20.4	18.6	23.8	25.2	24.1	0.25
Nd	34.2	37.8	31.9	28.9	26.3	32.5	34.5	28.3	31.2	31.1	27.8	34.8	110	96.1	132	125	139	0.86
Sm	13.4	16.2	12.9	11.4	10.6	12.6	13.6	10.2	12.2	12.6	11.2	14	32.8	31.2	43.3	43.4	38.3	0.96
Eu	3.49	4.43	3.56	3.47	2.93	3.29	3.82	2.88	3.31	3.42	3.1	3.84	8.39	8.2	9.91	8.21	9.27	0.25
Gd	17.7	19.7	16.53	15.4	14.7	16.5	18.7	14.5	17.6	16.8	14.8	18.8	30.6	29	35.5	35.4	36.6	0.65
Tb	3.24	3.59	3.01	2.76	2.8	2.98	3.41	2.82	3.04	3.16	3.04	3.53	5.5	4.77	6.59	5.91	6.62	0.23
Dy	21.7	26.0	20.9	19.5	19.0	20.7	24.2	19.2	21.9	22.3	19.7	24.1	32.2	39.6	43.6	39.2	41.9	0.57
Ho	4.93	5.34	4.54	4.23	4.13	4.38	5.29	4.05	5.09	5.07	4.21	5.21	6.9	6.71	7.94	7.62	8.38	0.08
Er	13.5	15.5	12.2	11.9	11.3	12.7	14.9	11.5	14.3	13.8	12.2	14.8	18.6	17.3	22.6	22.7	23.5	0.4
Tm	1.73	1.96	1.6	1.47	1.41	1.58	1.7	1.53	1.73	1.74	1.39	1.8	2.76	2.28	2.97	3.03	2.61	0.11
Yb	9.27	10.6	8.34	8.91	8.59	8.9	9.78	8.34	10.2	9.64	8.4	9.79	17.1	14.9	18.4	15.2	15.8	0.87
Lu	1	1.22	0.97	0.9	0.95	1.05	1.12	0.85	1.16	1.09	0.94	1.19	1.7	1.51	2.02	2.16	1.99	0.15
ΣREE	151	174	142	132	123	143	158	126	144	145	127	158	389	366	471	468	477	5.96
Y	479	152	129	123	122	131	146	117	141	141	119	142	141	126	161	155	163	0.78
Hf	5395	5297	5171	5219	5124	5122	5650	5735	5760	5437	5438	5473	16234	6815	11459	8440	8836	1.29
Ta	235	310	315	290	450	283	301	307	529	462	331	315	604	673	693	767	755	0.16
W	29.1	4.02	0.77	0.87	1.8	0.74	2.15	0.73	4.45	14.9	1.04	0.72	121	126	148	120	178	0.41

bdl: below detection limits. C: core. R: rim.

is mainly composed of TiO_2 (63 wt %–66 wt %), MgO (27 wt %–30 wt %), and FeO (5.2 wt %–7.0 wt %). The contents of UO_2 and ThO_2 in the three minerals above are lower than the limits of detection by EPMA analyses.

4.2.3 Silicate minerals and spinel

The compositions of silicate and oxide minerals (forsterite, spinel, and phlogopite) coexisting with zirconolite were analyzed, and the results are presented in Table S1. Forsterite has near-endmember compositions with X_{Mg} [$= Mg / (Mg + Fe^{2+})$] = 0.99. Spinel has high Al contents of 68 wt %–70 wt % and X_{Mg} of 0.98–0.90. The Cr_2O_3 contents of spinel range from 0.80 wt %–3.3 wt %. Phlogopite has near-endmember compositions ($X_{Mg} = 0.99$–1) and high TiO_2 contents of 0.57 wt %–1.5 wt %. The K (0.63–0.87 apfu, atomic proportion per formula unit) and Na (0.11–0.38 apfu) contents of phlogopite are high, and the Ca (≤ 0.002 apfu) contents are low. In addition, phlogopite contains considerable amounts of F (1.6 wt %–1.9 wt %).

4.3 U–Pb ages of zirconolite

The U–Th–Pb isotope contents of zirconolite are presented in Table S2 and shown in Fig. 10. The f_{206} values of zirconolite in the MMB range from 1 %–7 %, indicating low proportions of common Pb. The Th/U ratios of Zrl-I (0.03–0.08) and Zrl-II (0.04–0.08) are lower than those of Zrl-III (0.40–2.9). A total of 18 analyses on Zrl-I from sample 13MDL76-A and 16 analyses on Zrl-I from sample 13MDL76-B give lower intercept ages of 34.8 ± 0.5 Ma (2σ, mean square weighted deviation, MSWD = 1.7; Fig. 10a) and 35.2 ± 0.5 Ma (2σ, MSWD = 2; Fig. 10b), respectively, in Tera-Wasserburg concordia diagrams. Their weighted mean $^{206}Pb / ^{238}U$ ages after ^{207}Pb correction are 34.9 ± 0.5 Ma (2σ, MSWD = 1.6) and 35.3 ± 0.5 Ma (2σ, MSWD = 1.8), respectively. Four analyses on the 13MDL76-A Zrl-II and seven analyses on the 13MDL76-B Zrl-II yield lower intercept ages of 34.4 ± 1.0 Ma (2σ, MSWD = 0.17; Fig. 10c) and 34.9 ± 0.8 Ma (2σ, MSWD = 1.5; Fig. 10d), respectively. Their weighted mean $^{206}Pb / ^{238}U$ ages after ^{207}Pb correction are 34.4 ± 1.0 Ma (2σ, MSWD = 0.14) and 34.9 ± 0.8 Ma (2σ, MSWD = 1.1), respectively. There is no difference in the ages between the Zrl-II cores and rims. Six analyses of Zrl-III from 13MDL76-B define a regression line with a lower intercept age of 18.6 ± 0.9 Ma (2σ, MSWD = 1.1; Fig. 10e). The weighted mean $^{206}Pb / ^{238}U$ age after ^{207}Pb correction is 18.6 ± 0.9 Ma (2σ, MSWD = 0.92).

5 Discussion

5.1 Multiple growth of zirconolite in the reaction zones of marbles

The studied reaction zones in marbles were formed by episodic infiltrations of external reactive fluids (Guo et al., 2021). Thus, the growth of zirconolite in these reaction zones is associated with the different stages of fluid influx and mineral reactions.

Zrl-I occurs in the matrix and typically coexists with carbonates (calcite and dolomite), forsterite, spinel, and phlogopite, and it also contains calcite inclusions (Fig. 2a–f). The boundaries between Zrl-I and coexisting minerals are generally sharp, suggesting the simultaneous formation of these minerals. Therefore, Zrl-I developed during the first infiltration process that led to the metasomatic formation of forsterite, spinel, and phlogopite by the replacement of dolomite at 704–750 °C and ∼ 8 kbar (Guo et al., 2021). Zrl-I has very high ZrO_2 (28 wt %–30 wt %), TiO_2 (31 wt %–33 wt %), UO_2 (21 wt %–23 wt %), and ThO_2 (0.84 wt %–1.9 wt %) contents, and contain considerable amounts of Nb, Ta, and Hf (Table 1; Figs. 7c, 7d, 8c), indicating high contents of these elements in the K–Al–Si-bearing infiltrating fluid. This interpretation is in accordance with the petrographic observations that abundant rutile, uraninite, and baddeleyite occur in the reaction zones (Fig. 6), indicating high Zr–Ti–U contents in the reactive fluid. The metasomatic reactions involved in the formation of Zrl-I at the expense of dolomite can be summarized as follows:

$$\begin{aligned} &2\mathrm{Dol} + 4\mathrm{TiO_2(aq)} + \mathrm{ZrO_2(aq)} \\ &\quad = \mathrm{Zrl} + \mathrm{Cal} + 2\mathrm{Gk} + 3\mathrm{CO_2}, \end{aligned} \tag{R1}$$

$$\begin{aligned} &2\mathrm{Dol} + 2\mathrm{TiO_2(aq)} + \mathrm{ZrO_2(aq)} + \mathrm{SiO_2(aq)} \\ &\quad = \mathrm{Zrl} + \mathrm{Cal} + \mathrm{Fo} + 3\mathrm{CO_2}, \end{aligned} \tag{R2}$$

$$\begin{aligned} &2\mathrm{Dol} + 2\mathrm{TiO_2(aq)} + \mathrm{ZrO_2(aq)} + 2\mathrm{Al_2O_3} \\ &\quad = \mathrm{Zrl} + \mathrm{Cal} + 2\mathrm{Spl} + 3\mathrm{CO_2}, \end{aligned} \tag{R3}$$

$$\begin{aligned} &6\mathrm{Dol} + 2\mathrm{TiO_2(aq)} + \mathrm{ZrO_2(aq)} + \mathrm{Al_2O_3} + 6\mathrm{SiO_2} \\ &\quad + \mathrm{K_2O} + 2\mathrm{H_2O} = \mathrm{Zrl} + 5\mathrm{Cal} + 2\mathrm{Phl} + 7\mathrm{CO_2}, \end{aligned} \tag{R4}$$

$$\begin{aligned} &\mathrm{Dol} + 2\mathrm{TiO_2(aq)} + \mathrm{UO_2(aq)} \\ &\quad = \mathrm{U\text{-}Zrl(UZrTi_2O_7)} + \mathrm{Cal} + \mathrm{CO_2}, \end{aligned} \tag{R5}$$

$$\begin{aligned} &\mathrm{Dol} + 2\mathrm{TiO_2(aq)} + \mathrm{ThO_2(aq)} \\ &\quad = \mathrm{Th\text{-}Zrl(ThZrTi_2O_7)} + \mathrm{Cal} + \mathrm{CO_2}. \end{aligned} \tag{R6}$$

Zrl-II has a grain shape, size, and inclusions similar to those of Zrl-I. Both types of zirconolite have the same coexisting mineral assemblages. Moreover, Zrl-II cores have the same compositional variations and REE patterns as those of Zrl-I (Fig. 3d). Thus, we consider that the growth mechanism of Zrl-II cores is similar to that of Zrl-I. The formation of irregular Zrl-II rims is related to a later alteration process because the sharp core–rim contact of Zrl-II is consistent with fluid-assisted replacement reactions (e.g., Putnis and Austrheim, 2010).

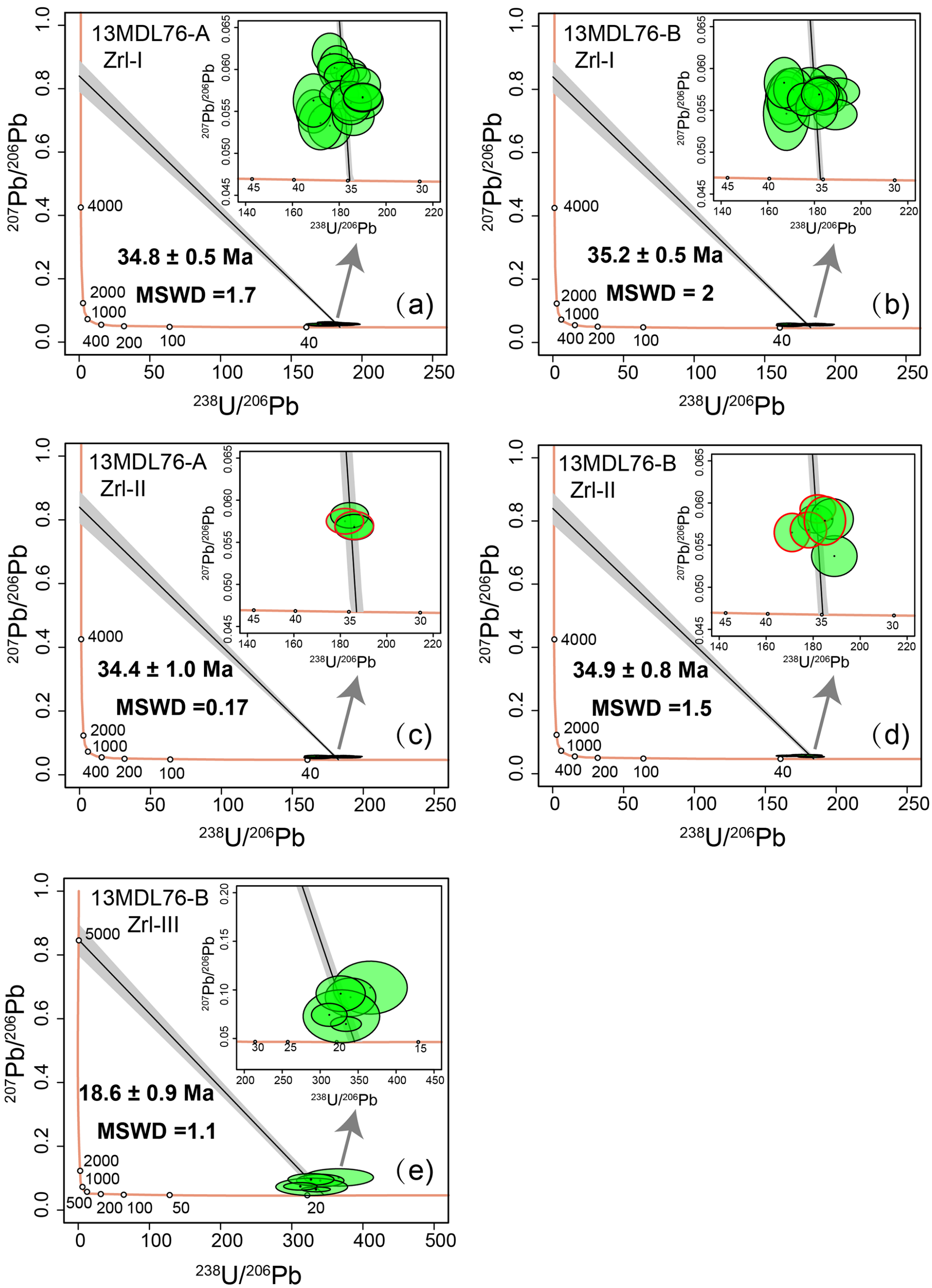

Figure 10. (a–b) Tera-Wasserburg U–Pb concordia diagrams for Zrl-I from 13MDL76-A **(a)** and 13MDL76-B **(b)**. **(c–d)** Tera-Wasserburg U–Pb concordia diagrams for Zrl-II from 13MDL76-A **(c)** and 13MDL76-B **(d)**. The red and black ellipses represent the core and rim of Zrl-II, respectively. **(e)** Tera-Wasserburg U–Pb concordia diagrams for Zrl-III from 13MDL76-B. The discordia lines in the Terra-Wasserburg diagrams are forced through a $^{207}Pb/^{206}Pb$ value of 0.84 ± 0.05. The $^{207}Pb/^{206}Pb$ values were estimated using the two-stage crustal Pb model of Stacey and Kramers (1975) for all samples. The gray areas in Tera-Wasserburg U–Pb concordia diagrams show that the variation in the estimated $^{207}Pb/^{206}Pb$ value has little effect on the calculated ages for low common Pb contents for Zrl-I and Zrl-II ($f_{206} < 2\,\%$, Table S2; Li et al., 2012). The data-point error bars are 1σ.

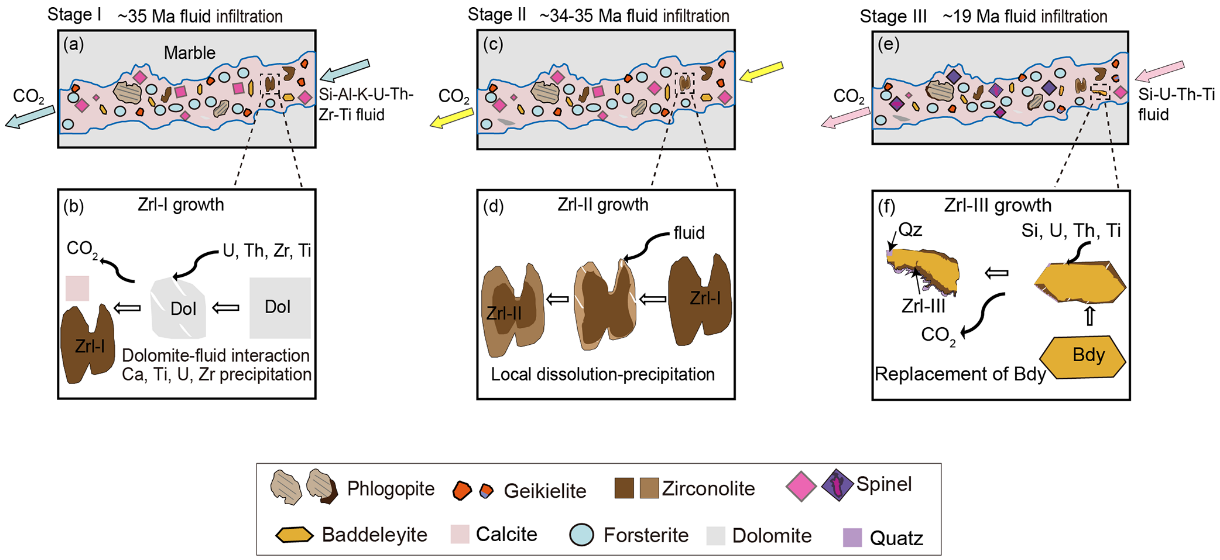

Figure 11. Schematic model (not-to-scale) of multiple episodes of fluid infiltration in the marbles **(a, c, e)** and the growth of Zrl-I **(b)**, Zrl-II **(d)**, and Zrl-III **(f)**.

The corona textures of Zrl-III around baddeleyite and the jagged grain boundaries between the two minerals (Fig. 4) indicate the growth of Zrl-III by the replacement of baddeleyite. Similar textures of zirconolite rimming baddeleyite have been previously observed in metacarbonate rocks (e.g., Purtscheller and Tessadri, 1985; Tropper et al., 2007), mafic–ultramafic magmatic rocks (e.g., Rasmussen and Fletcher, 2004; Azzone et al., 2009; Hurai et al., 2018), and lunar basalt (e.g., Rasmussen et al., 2008; Li et al., 2021). The formation of the Zrl-III corona is closely related to fluid metasomatism via a mechanism of interface-coupled dissolution–precipitation (ICDP) (e.g., Putnis and Austrheim, 2010; Guo et al., 2017). Zrl-III does not form on all the boundaries of baddeleyite (Fig. 4), suggesting that Zrl-III formed only on the sites where the infiltrating fluid was able to pass. Calcium in Zrl-III is locally derived from calcite, and Ti may be derived from the infiltrating fluid. The large compositional variation for the Zrl-III corona after a single baddeleyite grain (Fig. 4a, Table 1) may be caused by different degrees of fluid–mineral interaction and element exchange at different sites of the baddeleyite grain boundary. Based on the reactants and products, the following reaction can be inferred:

$$\mathrm{Bdy} + 2\mathrm{TiO_2(aq)} + \mathrm{CaCO_3} = \text{Zrl-III} + \mathrm{CO_2}. \qquad \text{(R7)}$$

Zrl-III has variable and much higher UO_2 (0.88 wt %–5.3 wt %) and ThO_2 (0.60 wt %–6.8 wt %) than baddeleyite ($UO_2 \leq 0.23$ wt %, $ThO_2 \leq 0.06$ wt %; Table S1), indicating that the infiltrating fluids responsible for Zrl-III also contain certain amounts of U and Th. However, the UO_2 contents of Zrl-III are obviously lower than those of Zrl-I and Zrl-II (Fig. 7a; Table 1), implying that the later-stage infiltrating fluid has lower UO_2 contents than the first-stage infiltrating fluid. Interestingly, Zrl-III is found to be intergrown with polycrystalline quartz (Figs. 4c, d and 5e). This phenomenon has rarely been reported in natural rocks (Rasmussen and Fletcher, 2004; Rasmussen et al., 2008, 2009). The coexistence of Zrl-III and quartz in the MMB samples indicates that this stage of the reactive fluid was locally SiO_2-saturated. Guo et al. (2021) revealed that a gneiss-derived later-stage fluid with high SiO_2 activity infiltrated the marbles at $\sim 680\,°C$ and 5 kbar. We therefore suggest that the development of Zrl-III is also associated with this stage of high-α_{SiO_2} fluid influx.

In summary, the above results indicate that the three types of zirconolite record multiple episodes of fluid infiltration in the marbles. The first stage of infiltration led to the formation of Zrl-I and Mg-rich silicates and oxides, as well as other accessory minerals (baddeleyite and geikielite) (Fig. 11a and b). The reactive K–Al–Si fluid was also enriched in Zr, Ti, U, and Th. After that, a portion of Zrl-I grains experienced a local fluid-assisted dissolution–precipitation process, producing a core–rim zonation (i.e., the Zrl-II type) (Fig. 11c and d). The final stage of infiltration formed Zrl-III at the expense of baddeleyite. This final stage of fluid was characterized by relatively low U contents and high SiO_2 activities (Fig. 11e and f).

5.2 Constraints on episodic infiltration by zirconolite U–Pb dating

The high U and Pb contents and low common Pb contents in zirconolite provide a good opportunity to elucidate the time-resolved infiltration history and episodic fluid–rock interactions in the marbles using in situ dating technology. The analyses of Zrl-I grains from both samples yield similar lower intercept ages of 34.8 ± 0.5 Ma (2σ, MSWD = 1.7,

$n = 18$; Fig. 10a) and 35.2 ± 0.5 Ma (2σ, MSWD = 2, $n = 16$; Fig. 10b), consistent with the U–Pb ages of baddeleyite cores (35.8 ± 0.8 Ma; Guo et al., 2021) in the same samples. This result further supports the simultaneous formation of Zrl-I and baddeleyite, and therefore the ages represent the time of the earliest infiltration event in these marbles. Because the Zrl-I ages are similar to the emplacement ages of hornblende syenites near the marbles (from 33.1 ± 0.9 to 30.9 ± 0.6 Ma; Barley et al., 2003), it is reasonable to infer that the Zr–Ti–U–Th-rich metasomatic fluid is derived from the syenitic magma (Searle et al., 2020).

Zrl-II from the two samples gives lower intercept ages of 34.4 ± 1.0 Ma (2σ, MSWD = 0.17, $n = 4$; Fig. 10c) and 34.9 ± 0.8 Ma (2σ, MSWD = 1.5, $n = 7$; Fig. 10d), which are in accordance with those of Zrl-I within the uncertainties. The ages of the Zrl-II cores and rims are indistinguishable within the uncertainties. Thus, Zrl-II most likely represents Zrl-I grains that have experienced a local dissolution–precipitation process, which occurred slightly later than the formation of Zrl-I (i.e., Zrl-II cores).

The analyses of the Zrl-III corona around baddeleyite yield a lower intercept age of 18.6 ± 0.9 Ma (2σ, MSWD = 1.1, $n = 6$; Fig. 10e), indicating an infiltration event postdating the formation of Zrl-I and Zrl-II. The ages are consistent with the time of the final stage of infiltration in the marbles constrained by zircon U–Pb dating (17.05 ± 0.27 Ma) in the same samples (Guo et al., 2021). The ages are also close to those of a biotite granite dike in the nearby Sedawgyi gneisses (17.0 ± 0.3 Ma; Mitchell et al., 2012). We thus suggest that the last stage of SiO_2-rich infiltrating fluids was derived from the partial melts of the gneisses during the Miocene uplift cooling process of the MMB (Bertrand et al., 1999, 2001; Garnier et al., 2006; Mitchell et al., 2012).

Therefore, the multiple formation stages of zirconolite record episodes of infiltration in the marbles ranging from 35 to 19 Ma during the India–Asia collision and uplift of the MMB (Fig. 11a–f).

5.3 Comparison with other types of zirconolite

Zirconolite occurs in a variety of rock types, including metasomatized metacarbonates, mafic–ultramafic magmatic rocks, carbonatites, syenite, syenite pegmatite, placer deposits, and extraterrestrial samples (see the review of Williams and Gieré, 1996). This mineral has several cation-acceptor sites, which allows a series of cation substitutions ranging in ionic radii from 0.40 to 1.14 A° and charges from 2^+ to 6^+ (Giereì et al., 1998). The compositions of natural zirconolite vary extensively, and the predominant substitutions involve (1) U, Th, Pb, and REEs for Ca; (2) Hf for Zr; and (3) Al, Nb, Ta, Fe, Mg, Mn, Zn, and W for Ti (Gieré et al., 1998). Clarifying the correlation between zirconolite compositions and types of host lithologies is essential to understand the mineral growth mechanism and element substitution, as well as to establish a potential framework to trace the origin of zirconolite.

The MMB zirconolite, which formed by the metasomatism of dolomite marbles, is characterized by high UO_2 (0.88 wt %–24 wt %) and ThO_2 (0.6 wt %–6.8 wt %) contents and low REE contents (below the detection limits by EPMA). The $U^{4+} + Th^{4+}$ content correlates well with the $Mg^{2+} + Fe^{2+}$ content (Fig. 7b), indicating that the following coupled substitution causes the U^{4+} and Th^{4+} enrichments in zirconolite (Giereì and Williams, 1992): $(U, Th)^{4+} + (Mg, Fe)^{2+} = Ca^{2+} + Ti^{4+}$. The positive correlation between $Nb^{5+} + Al^{3+}$ and Ti^{4+} (Fig. 7c) supports the fact that the enrichments of Nb (maybe also Ta) are mainly governed by the following coupled substitution: $(Nb, Ta)^{5+} + Al^{3+} = 2Ti^{4+}$ (Giereì and Williams, 1992). The incorporation of Hf in zirconolite is controlled by the substitution of $Hf^{4+} = Zr^{4+}$, as indicated by the positive correlation between the two elements (Fig. 7d).

Figure 8a–c compare the compositions of zirconolite from the MMB samples with those from a variety of lithologies reported in previous studies, including mafic–ultramafic magmatic rocks (kimberlites and lunar basalts), carbonatites, syenites, and metasomatized carbonate rocks. MMB zirconolite has similar contents of Ca, Ti, and Zr to other types of zirconolite (Fig. 8a). The U + Th contents of zirconolite are highly varied (from 0.002 to 0.48 apfu) for all types of lithologies except the lunar samples, the zirconolite of which typically has relatively low U + Th contents (< 0.013 apfu) (Fig. 8b). In contrast, different types of zirconolite have distinct REE + Y concentrations (Fig. 8b). Generally, zirconolite in syenites, lunar basalts, and mafic–ultramafic magmatic rocks have high total REE + Y contents (up to 0.65 apfu). Zirconolite formed during metasomatic processes of carbonate rocks (skarn) and marbles, including the MMB zirconolite, typically exhibits the lowest contents of REE + Y (from 0 to 0.20 apfu). The REEs contents of zirconolite from carbonatites and most mafic–ultramafic rocks are in between those of the syenites and metasomatic rocks. The Nb_2O_5 and HfO_2 contents for different types of zirconolites are also highly variable (Fig. 8c). Zirconolite from the metasomatic rocks and lunar samples generally have lower Nb_2O_5 contents than those from carbonatites and syenites.

5.4 Implication for multiple stages of infiltration in metacarbonates and Zr–Ti–Th–U mineralization

Fluid/melt infiltration into metacarbonates and fluid/melt-rock interactions occur widely in subduction–collision orogenic belts, which may induce significant CO_2 release and mineralization of critical metals (e.g., Stewart et al., 2018; Guo et al., 2021, 2022; Kerrick, 1977; Meinert et al., 2005; Deng and Wang, 2016; Xie et al., 2021). A growing number of studies have indicated that the infiltration–metasomatic processes in metacarbonates are complex and involve multiple episodes of reactions (e.g., Jamtveit et al., 1993; Satish-

Kumar et al., 2010; Brice et al., 2019; Tan et al., 2022; Guo et al., 2019, 2021; Zeng and Liu, 2022). However, it is difficult to precisely constrain the time and fluid chemical characteristics of each infiltration episode. Studies on zirconolite provide a new solution to address this problem. Our new results on the MMB reaction zones indicate that zirconolite can grow at various stages in response to the episodic fluid infiltrations and fluid-assisted replacement reactions. On the one hand, high U–Th–Pb contents and advances in the in situ isotopic analytical technique enable the zirconolite to yield the time of fluid influx (Sect. 5.2). On the other hand, compared to other accessory geochronometers (e.g., baddeleyite, zircon, and rutile) in metacarbonate rocks, zirconolite can accommodate more groups of trace elements in its crystal lattice (Sect. 5.3). Therefore, this mineral also provides more information on the compositions of introduced reactive fluids. Here, a comprehensive study on the MMB samples presents an example to elucidate the fluid influx history and reactive fluid compositions in the marbles using zirconolite. More importantly, the growth of zirconolite in metacarbonates is typically accompanied by the consumption of carbonates and the release of CO_2 (Reactions R1–R7). Thus, zirconolite may be of particular importance for characterizing the decarbonation process and the flow of carbonic fluids.

Our results indicate an efficient mobilization and transfer of Zr (Hf), Ti (Nb and Ta), and U (Th) during the fluid–rock interactions, although high-field-strength elements (HFSEs) were typically regarded as sparingly soluble components in aqueous fluids (e.g., Keppler and Wyllie, 1990, 1991; Audétat and Keppler, 2005; Tropper and Manning, 2005). Experimental and geological studies indicate that the enrichment of F and other halogens can significantly elevate the solubility of HFSEs by complexing with HFSEs in aqueous fluid (Keppler and Wyllie, 1990, 1991; Peiffer et al., 1996; Antignano and Manning, 2008; Cuney, 2009; Rapp et al., 2010; Bali et al., 2011; Migdisov et al., 2011; Tanis et al., 2016; Karmakar, 2021). The high F contents in phlogopite (1.6 wt %–1.9 wt %) from the reaction zones indicate that the reactive HFSE-bearing fluids also contain F. We thus suggest that F played an important role in transporting HFSEs in the fluids (Gieré, 1986; Salvi and WilliamsJones, 1996; Zhao et al., 2016; Guo et al., 2016; Duan and Li, 2017; Zeng and Liu, 2022), and the growth of phlogopite during the fluid–marble interaction decomposed F–HFSE complexes to deposit Zrl and other HFSE-rich minerals. In addition, we reveal that the mineralization of Zr–Ti–U-rich phases in (meta-)carbonate rocks could be episodic. This provides a new insight into the transport and precipitation of HFSEs during crustal fluid–rock interactions.

6 Conclusions

Three textural types of zirconolite (Zrl-I, Zrl-II, and Zrl-III), which formed by multiple episodes of fluid–marble interaction during the India–Asia continental collision, have been recognized in the reaction zones of MMB dolomite marbles. These types of zirconolite record important information about the timing of episodic infiltration and the chemical compositions of the reactive fluids. Zrl-I records the first episode of fluid infiltration at ~ 35 Ma with high U and Th contents in the reactive fluid. Zrl-II, which has a core–rim compositional zonation, reflects a local dissolution–precipitation process slightly later than the first episode of fluid infiltration. Zrl-III, which formed by the replacement of baddeleyite, documents a final stage of SiO_2-rich fluid infiltration at ~ 19 Ma. This late reactive fluid has lower U contents. All the infiltrating fluids have low REE contents. The fluids responsible for the Zrl-I and Zrl-II formation were derived from the syenite intrusions, whereas the fluid responsible for the formation of Zrl-III was associated with the granite dike in nearby gneisses. This study illustrates that the combination of detailed petrographic study, mineral chemistry, and in situ U–Pb dating on multistage-formed zirconolite can be used to constrain the time-resolved fluid infiltration history in metacarbonates and reactive fluid compositions.

Data availability. All data derived from this research are presented in the enclosed tables, figures, and Supplement.

Supplement. The supplement related to this article is available online at: https://doi.org/10.5194/ejm-36-11-2024-supplement.

Author contributions. SG collected the samples and designed the study. QG carried out detailed petrography, mineral chemistry, and U–Pb dating. SG and QG interpreted the data and prepared the manuscript. YY guided the U–Pb isotope data processing. QM, JY, and SW helped with EPMA, SEM, and trace element analyses, respectively. XL and KS participated in the discussion of data interpretation.

Competing interests. The contact author has declared that none of the authors has any competing interests.

Acknowledgements. The manuscript benefitted from helpful discussions with Xu Chu, Yi Chen, Chuan-Zhou Liu, and Jian-Gang Wang. We also thank Di Zhang, Lei Xu, and Qindi Wei for their help during the experiments.

Financial support. This study was financially supported by the National Key R&D Program of China (grant no. 2022YFF0800800); the second comprehensive scientific investigation into Qinghai–Tibet Plateau (grant no. 2019QZKK0802); the State Key Laboratory of Lithospheric Evolution (grant no. SKL-Z202002); the National Natural Science Foundation of China (grant no. 41903049); the Key Research Program of the Institute of Geology and Geophysics, CAS (grant no. IGGCAS-202204); and the Youth Innovation Promotion Association, CAS (grant no. Y2021026).

Review statement. This paper was edited by Encarnacion Ruiz-Agudo and reviewed by Penglei Liu and Rachelle Turnier.

References

Audétat, A. and Keppler, H.: Solubility of rutile in subduction zone fluids, as determined by experiments in the hydrothermal diamond anvil cell, Earth Planet. Sc. Lett., 232, 393–402, https://doi.org/10.1016/j.epsl.2005.01.028, 2005.

Antignano, A. and Manning, C.E.: Fluorapatite solubility in H2O and H_2O–NaCl at 700 to 900 °C and 0.7 to 2.0 GPa. Chem. Geol., 251, 112–119, https://doi.org/10.1016/j.chemgeo.2008.03.001, 2008.

Azzone, R. G., Ruberti, E., Enrich, G. E. R., and Gomes, C. B.: Zr- and Ba-rich minerals from the Ponte Nova alkaline mafic–ultramafic massif, southeastern Brazil: indication of an enriched mantle source, Can. Mineral., 47, 1087–1103, https://doi.org/10.3749/canmin.47.5.1087, 2009.

Bali, E., Audétat, A., and Keppler, H.: The mobility of U and Th in subduction zone fluids: an indicator of oxygen fugacity and fluid salinity, Contrib. Mineral. Petrol., 161, 597–613, https://doi.org/10.1007/s00410-010-0552-9, 2011.

Barker, S. L., Cox, S. F., Eggins, S. M., and Gagan, M. K.: Microchemical evidence for episodic growth of antitaxial veins during fracture-controlled fluid flow, Earth Planet. Sc. Lett., 250, 331–344, https://doi.org/10.1016/j.epsl.2006.07.051, 2006.

Barley, M. E., Doyle, M. G., Zaw, K., Pickard, A. L., and Rak, P.: Jurassic–Miocene magmatism and metamorphism in the Mogok metamorphic belt and the India-Eurasia collision in Myanmar, Tectonics, 22, 1–11, https://doi.org/10.1029/2002TC001398, 2003.

Bellatreccia, F., Della Ventura, G., William, T. C., Lumpkin, G. L., Smith, K. L., and Colella, M.: Non-metamict zirconolite polytypes from the feldspathoid-bearing alkalisyenitic ejecta of the Vico volcanic complex (Latium, Italy), Eur. J. Mineral., 14, 809–820, https://doi.org/10.1127/0935-1221/2002/0014-0809, 2002.

Bertrand, G., Rangin, C., Maluski, H., Han, T. A., Thein, M., Myint, O., Maw, W., and Lwin, S.: Cenozoic metamorphism along the Shan scarp (Myanmar): Evidences for ductile shear along the Sagaing fault or the northward migration of the eastern Himalayan syntaxis?, Geophys. Res. Lett., 26, 915–918, https://doi.org/10.1029/1999GL900136, 1999.

Bertrand, G., Rangin, C., Maluski, H., and Bellon, H.: Diachronous cooling along the Mogok metamorphic belt (Shan scarp, Myanmar): The trace of the northward migration of the Indian syntaxis, J. Asian Earth Sci., 19, 649–659, https://doi.org/10.1016/S1367-9120(00)00061-4, 2001.

Brice, L., Lukas, P.B., Anne Sophie, B., Pamela, D. K., and Torsten, V.: Multi fluid-flow record during episodic mode I opening: A microstructural and SIMS study (Cotiella Thrust Fault, Pyrenees), Earth Planet. Sc. Lett., 503, 37–46, https://doi.org/10.1016/j.epsl.2018.09.016, 2018.

Busche, F. D., Prinz, M., Kell, K., and Kurat G.: Lunar zirkelite: A uranium-bearing phase, Earth Planet. Sc. Lett., 14, 313–321, https://doi.org/10.1016/0012-821X(72)90130-6, 1972.

Carter, L. B. and Dasgupta, R.: Decarbonation in the Ca-Mg-Fe carbonate system at mid-crustal pressure as a function of temperature and assimilation with arc magmas – Implications for long-term climate, Chem. Geol., 492, 30–48, https://doi.org/10.1016/j.chemgeo.2018.05.024, 2018.

Chen, S., Chen, Y., Li, Y. B., Su, B., Zhang, Q. H., Aung, M. M., and Sein, K.: Cenozoic ultrahigh-temperature metamorphism in pelitic granulites from the Mogok metamorphic belt, Myanmar, Sci. China Earth Sci., 64, 1873–1892, https://doi.org/10.1007/s11430-020-9748-5, 2021.

Cuney, M.: The extreme diversity of uranium deposits, Miner. Deposits, 44, 3–9, https://doi.org/10.1007/s00126-008-0223-1, 2009.

Deng, J. and Wang, Q. F.: Gold mineralization in China: Metallogenic provinces, deposit types and tectonic framework, Gondwana Res., 36, 219–274, https://doi.org/10.1016/j.gr.2015.10.003, 2016.

Deng, X. D., Li, J. W., and Wen, G.: Dating iron skarn mineralization using hydrothermal allanite-(La) U-Th-Pb isotopes by laser ablation ICP-MS, Chem. Geol., 382, 95–110, https://doi.org/10.1016/j.chemgeo.2014.05.023, 2014.

Duan, Z. and Li, J.W.: Zircon and titanite U-Pb dating of the Zhangjiawa iron skarn deposit, Luxi district, North China Craton: Implications for a craton-wide iron skarn mineralization, Ore Geol. Rev., 89, 309–323, https://doi.org/10.1016/j.oregeorev.2017.06.022, 2017.

Evans, K.: Metamorphic carbon fluxes: how much and how fast?, Geology, 39, 195–196, 2011.

Ferry, J. M.: Fluids in the crust during regional metamorphism: Forty years in the Waterville limestone, Am. Mineral., 101, 500–517, https://doi.org/10.2138/am-2016-5118, 2016.

Gardiner, N. J., Searle, M. P., Robb, L. J., and Morley, C. K.: Neo-Tethyan magmatism and metallogeny in Myanmar – An Andean analogue?, J. Asian Earth Sci., 106, 197–215, https://doi.org/10.1016/j.jseaes.2015.03.015, 2015.

Garnier, V., Maluski, H., Giuliani, G., Ohnenstetter, D., and Schwarz, D.: Ar-Ar and U-Pb ages of marble-hosted ruby deposits from central and southeast Asia, Can. J. Earth Sci., 43, 509–532, https://doi.org/10.1139/E06-005, 2006.

Gieré, R.: Zirconolite, allanite and hoegbomite in a marble skarn from the Bergell contact aureole: implications for mobility of Ti, Zr and REE, Contrib. Mineral. Petrol., 93, 459–470, https://doi.org/10.1007/BF00371716, 1986.

Gieré, R.: Transport and deposition of REE in H_2S-rich fluids: evidence from accessory mineral assemblages, Chem. Geol., 110, 251–268, https://doi.org/10.1016/0009-2541(93)90257-J, 1990.

Gieré, R. and Williams, C. T.: REE-bearing minerals in a Ti-rich vein from the Adamello contact aureole (Italy), Contrib. Mineral. Petrol., 112, 83–100, https://doi.org/10.1007/BF00310957, 1992.

Gieré, R., Williams, C. T., and Lumpkin, G.: Chemical characteristics of natural zirconolite, Schweiz, Mineral. Petrogr. Mitt., 78, 433–459, 1998.

Griffin, W., Powell, W., Pearson, N. J., and O'Reilly, S. Y.: GLITTER: data reduction software for laser ablation ICP-MS, in: Laser Ablation-ICP-MS in the Earth Sciences: Current Practices and Outstanding Issues, edited by: Sylvester, P., Mineral. Assoc. Can., Short Course, 40, 308–311, 2008.

Guo, S., Chen, Y., Liu, C. Z., Wang, J. G., Su, B., Gao, Y. J., Wu, F. Y., Sein, K., Yang, Y. H., and Mao, Q.: Scheelite and coexisting F-rich zoned garnet, vesuvianite, fluorite in calc-silicate rocks from the Mogok metamorphic belt, Myanmar: Implications for metasomatism in marble and the role of halogens in W mobilization and mineralization, J. Asian Earth Sci., 117, 82–106, https://doi.org/10.1016/j.jseaes.2015.12.004, 2016.

Guo, S., Tang, P., Su, B., Chen, Y., Ye, K., Zhang, L. M., Gao, Y. J., Liu, J. B., and Yang, Y. H.: Unusual replacement of Fe-Ti oxides by rutile during retrogression in amphibolite-hosted veins (Dabie UHP terrane): A mineralogical record of fluid-induced oxidation processes in exhumed UHP slabs, Am. Mineral., 102, 2268–2283, https://doi.org/10.2138/am-2017-6120, 2017.

Guo, S., Zhao, K. D., John, T., Tang, P., Chen, Y., and Su, B.: Metasomatic flow of metacarbonate-derived fluids carrying isotopically heavy boron in continental subduction zones: Insights from tourmaline-bearing ultra-high pressure eclogites and veins (Dabie terrane, eastern China), Geochim. Cosmochim. Ac., 253, 159–200, https://doi.org/10.1016/j.gca.2019.03.013, 2019.

Guo, S., Chu, X., Hermann, J., Chen, Y., Li, Q. L., and Wu, F. Y.: Multiple episodes of fluid infiltration along a single metasomatic channel in metacarbonates (Mogok metamorphic belt, Myanmar) and implications for CO_2 release in orogenic belts, J. Geophys. Res., 126, e2020JB020988, https://doi.org/10.1029/2020JB020988, 2021.

Guo, S., Hermann, J., Tang, P., Chu, X., Chen, Y., and Su, B.: Formation of carbon-bearing silicate melts by melt-metacarbonate interaction at convergent plate margins, Earth Planet. Sc. Lett., 597, 117816, https://doi.org/10.1016/j.epsl.2022.117816, 2022.

Haifler, J., Skoda, R., Filip, J., Larsen, A. O., and Rohlicek, J.: Zirconolite from Larvik Plutonic Complex, Norway, its relationship to stefanweissite and nöggerathite, and contribution to the improvement of zirconolite end-member systematics, Am. Mineral., 106, 1255–1272, https://doi.org/10.2138/am-2021-7510, 2017.

Hurai, V., Huraiova, M., Gajdosova, M., Konecny, P., Slobodnik, M., and Siegfried, P. R.: Compositional variations of zirconolite from the Evate apatite deposit (Mozambique) as an indicator of magmatic-hydrothermal conditions during post-orogenic collapse of Gondwana, Miner. Petrol., 112, 279–296, https://doi.org/10.1007/s00710-017-0538-7, 2018.

Jamtveit, B., Wogelius, R. A., and Fraser, D. G.: Zonation patterns of skarn garnets: Records of hydrothermal system evolution, Geology, 21, 113–116, 1993.

Karmakar, S.: Formation of clinohumite ± spinel in dolomitic marbles from the Makrohar Granulite Belt, Central India: Evidence for Ti mobility during regional metamorphism, Am. Mineral., 102, 1818–1827, https://doi.org/10.2138/am-2021-7755, 2021.

Keppler, H. and Wyllie, P. J.: Role of fluids in transport and fractionation of uranium and thorium in magmatic provinces, Nature, 348, 521–533, https://doi.org/10.1038/348531a0, 1990.

Keppler, H. and Wyllie, P. J.: Partitioning of Cu, Sn, Mo, W, U, and Th between melt and aqueous fluid in the systems haplogranite-H_2O-HCl and haplogranite-H_2O-HF, Contrib. Mineral. Petrol., 109, 139–150, https://doi.org/10.1007/BF00306474, 1991.

Kerrick, D. M.: The genesis of zoned skarns in the Sierra Nevada, California, J. Petrol., 18, 144–181, https://doi.org/10.1093/petrology/18.1.144, 1977.

Lamont, T. N., Searle, M. P., Hacker, B. R., Kyi Htun, K., Htun, K. M, Morley C. K., Waters, D. J., and White, R. W.: Late Eocene-Oligocene granulite facies garnet-sillimanite migmatites from the Mogok Metamorphic belt, Myanmar, and implications for timing of slip along the Sagaing Fault, Lithos, 386/387, 106027, https://doi.org/10.1016/j.lithos.2021.106027, 2021.

Li, Q. L., Zhou, Q., Liu, Y., Xiao, Z. Y., Lin, Y. T., Li, J. H., Ma, H. X., Tang, G. Q., Guo, S., Tang, X., Yuan, J. Y., Li, J., Wu, F. Y., Ouyang, Z. Y., Li, C. L., and Li, X. H.: Two billion-year-old volcanism on the moon from Chang'E-5 basalts, Nature, 600, 54–58, https://doi.org/10.1038/s41586-021-04100-2, 2021.

Lorand, J. P. and Cottin, J. Y.: A new natural occurrence of zirconolite ($CaZrTi_2O_7$) and baddeleyite (ZrO_2) in basic cumulates: the Laouni layered intrusion (Southern Hoggar, Algeria), Mineral. Mag., 51, 671–676, https://doi.org/10.1180/minmag.1987.051.363.06, 1987.

Meinert, L. D.: Skarns and skarn deposits, Geosci. Can., 19, 145–162, 1992.

Meinert, L. D., Dipple, G. M., and Nicolescu, S.: World skarn deposit, Econ. Geol., 100th Anniversary Volume, 299–336, ISBN: 978-1-887483-01-8, 2005.

Melluso, L., Guarino, V., Lustrino, M., Morra, V., and Gennaro, R. D.: The REE- and HFSE-bearing phases in the Itatiaia alkaline complex (Brazil) and geochemical evolution of feldspar-rich felsic melts, Mineral. Mag., 81, 217–250, https://doi.org/10.1180/minmag.2016.080.122, 2017.

Migdisov, A. A., Williams-Jones, A. E., van Hinsberg, V., and Salvi, S.: An experimental study of the solubility of baddeleyite (ZrO_2) in fuoride-bearing solutions at elevated temperature, Geochim. Cosmochim. Ac., 75, 7426–7434, https://doi.org/10.1016/j.gca.2011.09.043, 2011.

Mitchell, A. H. G., Htay, M. T., Htun, K. M., Win, M. N., Oo, T., and Hlaing, T.: Rock relationships in the Mogok metamorphic belt, Tatkon to Mandalay, central Myanmar, J. Asian Earth Sci., 29, 891–910, https://doi.org/10.1016/j.jseaes.2006.05.009, 2007.

Mitchell, A., Chung, S.L., Oo., T., Lin, T. H., and Hung, C. H.: Zircon U-Pb ages in Myanmar: Magmatic-metamorphic events and the closure of a neo-Tethys ocean?, J. Asian Earth Sci., 56, 1–23, https://doi.org/10.1016/j.jseaes.2012.04.019, 2012.

Pascal, M. L., Di Muro, A., Fonteilles, M., and Principe, C.: Zirconolite and calzirtite in banded forsterite-spinel-calcite skarn ejecta from the 1631 eruption of Vesuvius: inferences for magma-wallrock interactions, Mineral. Mag., 73, 333–56, https://doi.org/10.1180/minmag.2009.073.2.333, 2009.

Pearce, N. J. G., Perkins, W. T., Westgate, J. A., Gorton, M. P., Jackson, S. E., Neal, C. R., and Chenery, S. P.: A compilation of new and published major and trace element data for NIST SRM 610 and NIST SRM 612 glass reference materials, Geostand. Newsl., 21, 115–144, https://doi.org/10.1111/j.1751-908X.1997.tb00538.x, 1997.

Peiffert, C., Cuney, M., and Nguyen-Trung, C.: Uranium in granitic magmas: Part 2. experimental determination of uranium solubility and fluid-melt partitioning coefficients in the uranium oxide-haplogranite-H_2O-NaX (X = Cl, F) system at 770 °C 2 kbar, Geochim. Cosmochim. Ac., 60, 1515–1529, https://doi.org/10.1016/0016-7037(96)00039-7, 1996.

Phyo, M. M., Wang, H. A. O., Guillong, M., Berger, A., Franz, L., Balmer, W. A., and Krzemnicki, M. S.: U-Pb dating of zircon and zirconolite inclusions in marble-hosted gem-quality ruby and spinel from Mogok, Myanmar, Minerals, 10, 195, https://doi.org/10.3390/min10020195, 2020.

Platt, R. G., Wall, F., Williams, C. T., and Wooley, A. R.: Zirconolite, chevkinite and other rare earth minerals from nepheline syenites and peralkaline granites and syenites of the Chilwa alkaline province, Malawi, Mineral. Mag., 51, 253–263, https://doi.org/10.1180/minmag.1987.051.360.07, 1987.

Proyer, A., Baziotis, I., Mposkos, E., and Rhede, D.: Ti- and Zr-minerals in calcite-dolomite marbles from the ultrahigh-pressure Kimi Complex, Rhodope mountains, Greece: Implications for the P-T evolution based on reaction textures, petrogenetic grids, and geothermobarometry, Am. Mineral., 99, 1429–1448, https://doi.org/10.2138/am.2014.4710, 2014.

Purtscheller, F. and Tessadri, R.: Zirconolite and baddeleyite from metacarbonates of the Ötztal-Stubai complex (northern Tyrol, Austria), Mineral. Mag., 49, 523–529, 1985.

Putnis, A. and Austrheim, H.: Fluid-induced processes: Metasomatism and metamorphism, Geofluids, 10, 254–269, https://doi.org/10.1111/j.1468-8123.2010.00285.x, 2010.

Rapp, J. F., Klemme, S., Butler, I. B., and Harley, S. L.: Extremely high solubility of rutile in chloride and fluoride-bearing metamorphic fluids: an experimental investigation, Geology, 38, 323–326, https://doi.org/10.1130/G30753.1, 2010.

Rasmussen, B. and Fletcher, I. R.: Zirconolite: a new U-Pb chronometer for mafic igneous rocks, Geology, 32, 785–788, 2004.

Rasmussen, B., Fletcher, I. R., and Muhling, J. R.: Pb / Pb geochronology, petrography and chemistry of Zr-rich accessory minerals (zirconolite, tranquillityite and baddeleyite) in mare basalt 10047, Geochim. Cosmochim. Ac., 72, 5799–5818, https://doi.org/10.1016/j.gca.2008.09.010, 2008.

Rasmussen, B., Mueller, A. G., and Fletcher, I. R.: Zirconolite and xenotime U-Pb age constraints on the emplacement of the Golden Mile Dolerite sill and gold mineralization at the Mt Charlotte mine, Eastern Goldfields Province, Yilgarn Craton, Western Australia, Contrib. Mineral. Petrol., 157, 559–572, https://doi.org/10.1007/s00410-008-0352-7, 2009.

Rajesh, V. J., Yokoyama, K., Santosh, M., Arai, S., Oh, C. W., and Kim, S. W.: Zirconolite and baddeleyite in an ultramafic suite from Southern India: early Ordovician carbonatite-type melts associated with extensional collapse of the Gondwana crust, J. Geol., 114, 171–188, https://doi.org/10.1086/499571, 2006.

Rocholl, A.: Major and trace element composition and homogeneity of microbeam reference material: Basalt glass USGS BCR-2G, Geostand. Newsl., 22, 33–45, https://doi.org/10.1111/j.1751-908X.1998.tb00543.x, 1998.

Salvi, S. and WilliamsJones, A. E.: The role of hydrothermal processes in concentrating high-field strength elements in the Strange Lake peralkaline complex, northeastern Canada, Geochim. Cosmochim. Ac., 60, 1917–1932, https://doi.org/10.1016/0016-7037(96)00071-3, 1996.

Satish-Kumar, M., Hermann, J., Miyamoto, T., and Osanai Y.: Fingerprinting a multistage metamorphic fluid–rock history: Evidence from grain scale Sr, O and C isotopic and trace element variations in high-grade marbles from East Antarctica, Lithos, 114, 217–228, https://doi.org/10.1016/j.lithos.2009.08.010, 2010.

Searle, M. P., Noble, S. R., Cottle, J. M., Waters, D. J., Mitchell, A. H. G., Hlaing, T., and Horstwood, M. S. A.: Tectonic evolution of the Mogok metamorphic belt, Burma (Myanmar) constrained by U-Th-Pb dating of metamorphic and magmatic rocks, Tectonics, 26, TC3014, https://doi.org/10.1029/2006TC002083, 2007.

Searle, M. P., Morley, C. K., Waters, D. J., Gardiner, N. J., Htun, U. K., and Nu, T. T.: Tectonic and metamorphic evolution of the Mogok Metamorphic and Jade Mines belts and ophiolitic terranes of Burma (Myanmar), Geol. Soc. Lond. Memoirs, 48, 261–293, https://doi.org/10.1144/M48.12, 2017.

Searle, M. P., Garber, J. M., Hacker, B. R., Htun, K., Gardiner, N. J., Waters, D. J., and Robb, L. J.: Timing of syenite-charnockite magmatism and ruby and sapphire metamorphism in the Mogok valley region, Myanmar, Tectonics, 39, e2019TC005998, https://doi.org/10.1029/2019TC005998, 2020.

Shi, G. H., Zhang, X. C., Wang, Y., Li, Q. L., Wu, F. Y., and He, H. Y.: Age determination of oriented rutile inclusions in sapphire and of moonstone from the Mogok metamorphic belt, Myanmar. Am. Miner., 106, 1852–1859, https://doi.org/10.2138/am-2021-7487, 2021.

Stacey, J. S. and Kramers, J. D.: Approximation of terrestrial lead isotope evolution by a two-stage model, Earth. Planet. Sc. Lett., 26, 207–221, https://doi.org/10.1016/0012-821X(75)90088-6, 1975.

Stewart, E. M., Ague, J. J., Ferry, J. M., Schiffries, C. M., Tao, R. B., Isson, T. T., and Planavsky, N. J.: Carbonation and decarbonation reactions: Implications for planetary habitability, Am. Mineral., 104, 1369–1380, https://doi.org/10.2138/am-2019-6884, 2019.

Stucki, A., Trommsdorff, V., and Günther, D.: Zirconolite in metarodingites of Penninic Mesozoic ophiolites, Central Alps, Schweiz. Mineral. Petrogr. Mitt., 81, 257–265, 2001.

Sun, S. S. and McDonough, W. F.: Chemical and isotopic systematics of oceanic basalts: Implications for mantle composition and processes, Geol. Soc. Spec. Publ., 42, 313–345, https://doi.org/10.1144/GSL.SP.1989.042.01.19, 1989.

Tan, W., Steven, M., Reddy, S. M., Fougerouse, D., Wang, C. Y., Xian, H. Y., Yang, Y. P., and He, H. P.: Superimposed microstructures of pyrite in auriferous quartz veins as fingerprints of episodic fluid infiltration in the Wulong Lode gold deposit, NE China, Mineral. Deposita, 57, 685–700, https://doi.org/10.1007/s00126-022-01104-4, 2022.

Tanis, E. A., Simon, A., Zhang, Y. X., Chow, P., Xiao, Y. M., Hanchar, J. M., Tschauner, O., and Shen, G. Y.: Rutile solubility in NaF–NaCl–KCl-bearing aqueous fluids at 0.5–2.79 GPa and 250–650 °C, Geochim. Cosmochim. Ac., 177, 170–181, https://doi.org/10.1016/j.gca.2016.01.003, 2016.

Themelis, T.: Gems and mines of Mogok, Bangkok: A and T Publishers, 352, ISBN 0940965-30-5, 2008.
Thu, Y. K. and Enami, M.: Evolution of metamorphic fluid recorded in granulite facies metacarbonate rocks from the middle segment of the Mogok metamorphic belt in central Myanmar, J. Metamorph. Geol., 36, 905–931, https://doi.org/10.1111/jmg.12419, 2018.
Tropper, P., Harlov, D., Krenn, E., Finger, F., Rhede, D., and Bernhard, F.: Zr-bearing minerals as indicators for the polymetamorphic evolution of the eastern, lower Austroalpine nappes (Stubenberg Granite contact aureole, Styria, Eastern Alps, Austria), Lithos, 95, 72–86, https://doi.org/10.1016/j.lithos.2006.07.008, 2007.
Tropper, P. and Manning, C. E.: Very low solubility of rutile in H2O at high pressure and temperature, and its implications for Ti mobility in subduction zones, Am. Mineral., 90, 502–505, https://doi.org/10.2138/am.2005.1806, 2005.
Ventura, G. D., Bellatreccia, F., and Willianms, C. T.: Zirconolite with significant REEZrNb(Mn, Fe)O_7 from a xenolith of the Laacher See eruptive center, Eifel volcanic region, Germany, Can. Mineral., 38, 57–65, https://doi.org/10.2113/gscanmin.38.1.57, 2000.
Vermeesch, P.: Isoplot R: A free and open toolbox for geochronology, Geosci. Front., 9, 1479–1493, https://doi.org/10.1016/j.gsf.2018.04.001, 2018.
Wang, N., Mao, Q., Zhang, T., Jialong Hao, J. L., and Lin, Y. T.: Nano SIMS and EPMA dating of lunar Zirconolite, Prog. Earth. Pl. Sci., 8, 51, https://doi.org/10.1186/s40645-021-00446-3, 2021.
Williams, C. T.: Uranium-enriched minerals in mesostasis areas of the rhum layered pluton, Contrib. Mineral. Petrol., 66, 29–39, https://doi.org/10.1007/BF00376083, 1978.
Williams, C. T. and Gieré, R.: Zirconolite: A review of localities worldwide, and a compilation of its chemical compositions, Bulletin of the Natural History Museum, London (Geology), 52, 1–24, 1996.
Win, M. M., Enami, M., and Kato, T.: Metamorphic conditions and CHIME monazite ages of Late Eocene to Late Oligocene high-temperature Mogok metamorphic rocks in central Myanmar, J. Asian Earth Sci., 117, 304–316, https://doi.org/10.1016/j.jseaes.2015.11.023, 2016.
Whitney, D. L., and Evans, B. W.: Abbreviations for names of rock-forming minerals, Am. Mineral., 95, 185–187, https://doi.org/10.2138/am.2010.3371, 2010.
Wu, F. Y., Yang Y. H., Mitchell, R. H., Bellatreccia, F., Li, Q. L., and Zhao, Z. F.: In situ U-Pb and Nd-Hf-(Sr) isotopic investigations of zirconolite and calzirtite, Chem. Geol., 277, 178–195, https://doi.org/10.1016/j.chemgeo.2010.08.007, 2010.
Wu, S. T., Karius, V., Schmidt, B. C., Simon, K., and Woerner, G.: Comparison of ultrafine powder pellet and flux-free fusion glass for bulk analysis of granitoids by laser ablation-inductively coupled plasma-mass Spectrometry, Geostand. Geoanal. Res., 42, 575–591, https://doi.org/10.1111/ggr.12230, 2018.
Wu, S. T., Worner, G., Jochum, K. P., Stoll, B., Simon, K., and Kronz, A.: The preparation and preliminary characterisation of three synthetic andesite reference glass materials (ARM-1, ARM-2, ARM-3) for In Situ Microanalysis, Geostand. Geoanal. Res., 43, 567–584, https://doi.org/10.1111/ggr.12301, 2019.
Wu, S. T., Yang, Y. H., Jochum, K. P., Romer, R. L., Glodny, J., Savov, I. P., Agostini, S., De Hoog, J. C. M., Stefan, T. M., Peters, S. T. M., Kronz, A., Zhang, C., Bao, Z., Wang, X. J., Li, Y. L., Tang, G. Q., Feng, L. J., Yu, H. M, Li, Z. X., Zhang, L., Lin, J., Zeng, Y., Xu, C. X., Wang, Y. P., Cui, Z., Deng, L., Xiao, J., Liu, Y. H., Xue, D. S., Zhang, D., Jia, L. H., Wang, H., Xu, L., Huang, C., Xie, L. W., Pack, A., Worner, G., He, M. Y., Li, C. F., Yuan, H. L., Huang, F., Li, Q. L., Yang, J. H., Li, X. H., and Wu, F. Y.: Isotopic compositions (Li-B-Si-O-Mg-Sr-Nd-Hf-Pb) and $Fe_2^+ / \Sigma Fe$ ratios of three synthetic andesite glass reference materials (ARM-1, ARM-2, ARM-3), Geostand. Geoanal. Res., 45, 719–745, https://doi.org/10.1111/ggr.12399, 2021.
Xie, L. W., Zhang, Y. B., Zhang, H. H., Sun, J. F., and Wu, F. Y.: In situ simultaneous determination of trace elements, U-Pb and Lu-Hf isotopes in zircon and baddeleyite, Chin. Sci. Bull., 53, 1565–1573, https://doi.org/10.1007/s11434-008-0086-y, 2008.
Xie, Q. H., Zhang, Z. C., Jin Z. L., Santosh, M., Han, L., Wang, K. Y., Zhao P. L., and He, H. H.: The high-grade Fe skarn deposit of Jinling, North China Craton: Insights into hydrothermal iron mineralization, Ore Geol. Rev., 138, 104395, https://doi.org/10.1016/j.oregeorev.2021.104395, 2021.
Yonemura, K., Osanai, Y., Nakano, N., Adachi, T., Charusiri, P., and Zaw, T. N.: EPMA U-Th-Pb monazite dating of metamorphic rocks from the Mogok Metamorphic belt, Central Myanmar, J. Mineral. Petrol. Sci., 198, 184–188, https://doi.org/10.2465/jmps.121019a, 2013.
Yuan, S., Peng, J., Hu, R., Li, H., Shen, N., and Zhang, D.: A precise U-Pb age on cassiterite from the Xianghualing tin-polymetallic deposit (Hunan, South China), Mineral. Deposita, 43, 375–382, https://doi.org/10.1007/s00126-007-0166-y, 2008.
Zaccarini, F., Stumpfl, E., and Garuti, F.: Zirconolite and Zr-Th-U minerals in chromitites of the Finero Complex, Western Alps, Italy: evidence for carbonatite-type metasomatism in a subcontinental mantle plume, Can. Mineral., 42, 1825–1845, https://doi.org/10.2113/gscanmin.42.6.1825, 2004.
Zeng, Z. Y. and Liu, Y.: Magmatic-hydrothermal zircons in syenite: A record of Nb–Ta mineralization processes in the Emeishan large igneous province, SW China, Chem. Geol., 589, 120675, https://doi.org/10.1016/j.chemgeo.2021.120675, 2022.
Zhang, D., Guo, S., Chen, Y., Li, Q. L., Ling, X. X., Liu, C. Z., and Sein, K.: ∼ 25 Ma Ruby mineralization in the Mogok stone tract, Myanmar: new evidence from SIMS U-Pb dating of coexisting titanite, Minerals, 11, 536, https://doi.org/10.3390/min11050536, 2021.
Zhang, Y., Song, S. L., Hollings, P., Li, D. F., Shao, Y. J., Chen, H. Y., Zhao L. J., Kamo, S., Jin, T. T., Yuan, L. L., Liu, Q. Q., and Chen, S. C.: In-situ U-Pb geochronology of vesuvianite in skarn deposits, Chem. Geol., 612, 121136, https://doi.org/10.1016/j.chemgeo.2022.121136, 2022.
Zhao, W. W., Zhou, M. F., and Chen, W. T.: Growth of hydrothermal baddeleyite and zircon in different stages of skarnization, Am. Mineral., 101, 2689–2700, https://doi.org/10.2138/am-2016-5706, 2016.